Structure, surface and reactivity of activated carbon: From model soot to Bio Diesel soot

Hailong Zhang, Shanshan Li, Yi Jiao, Eduard Emil Iojoiu, Patrick da Costa, Maria Elena Galvez, Yaoqiang Chen

Structure, surface and reactivity of activated carbon: From model soot to Bio Diesel soot

Hailong Zhang[1,2], Shanshan Li[3], Yi Jiao[4], Eduard Emil iojoiu[5], Patrick Da Costa[1], Maria Elena Galvez[1], Yaoqiang Chen[6]

[1]Sorbonne Université, Institut Jean Le Rond d'Alembert, CNRS, 2 place de la gare de Ceinture, 78210 Saint Cyr L'Ecole, France

[2]College of Chemical Engineering, Sichuan University, Chengdu 610064, PR China

[3]State Key Laboratory of Polymer Materials Engineering of China (Sichuan University), Polymer Research Institute of Sichuan University, Chengdu 610065, PR China

[4]Institute of New Energy and Low-Carbon Technology, Sichuan University, Chengdu 610064, PR China

[5]Renault Trucks - Volvo Group Trucks Technology, Powertrain Engineering, 99 route de Lyon – 69806 Saint-Priest Cedex, France

[6]College of Chemistry, Sichuan University, Chengdu 610064, PR China

Corresponding authors:

catalysis5785@126.com (Hailong Zhang)

patrick.da_costa@sorbonne-universite.fr (Patrick Da Costa)

Abstract

The present work aims to investigate and compare the structure, surface and reactivity of the activated Printex U carbon black and real Bio soot samples through BET, Raman, HRTEM, XPS, DRIFTS and temperature-programmed oxidation (TPO). TPO evidenced that the activated Printex U carbon black was more reactive than the activated Biodiesel soot (B7 and B100) generated from a real engine under both O_2 and NO + O_2. BET displayed an increased surface area and a decreased pore size for the activated soot. Raman and HRTEM revealed that the activated soot showed decreased structural order. The morphology features also confirmed different

combustion pathway for Printex U and B100. XPS illustrated that the activation decreased surface graphene carbon and increased surface oxygen content. DRIFTS indicated that real Bio soot had higher concentration of surface functional groups than Printex U model soot, and a more apparent increase in surface functional groups was observed for the activated Printex U soot. It was proved that the reactivity of the activated Printex U is more dependent on structural and surface properties compared with that of the activated Biodiesel soot samples.

Keywords: Biodiesel soot; Nanostructure; Soot activation; Surface property; Soot oxidation reactivity

1. Introduction

The high efficiency and durability of Diesel engines have motivated their wide applications in passenger cars and heavy-duty trucks in the world. However, the incomplete combustion of fuel or poor fuel/air (F/A) mixing in Diesel engine has caused higher emission of fine soot particles for example $PM_{2.5}$, thereby leading to serious public health and environment pollution [1-4]. These fine soot particles as an important fraction of aerosols present in the air around urban area with big influences on the climate, biosphere and citizen health [5-9]. Diesel particulate matter (PM) mainly consists of carbon components, which include elemental carbon (EC), organic carbon (OC), and carbonate carbon (CC), the former two have an important impact on human health [10]. Polycyclic aromatic hydrocarbons (PAHs) as a class of OC are toxic and can readily condense onto PM under exhaust conditions. The presence of PAHs in air has been proven to be a key factor that leads to an increase in number of cancer cases [11-13].

Nowadays, the emissions of Diesel soot particles are limited all around world [14-17]. For example, the emissions of particulate matter from cars and heavy-duty vehicles are limited to 4.5 mg/km and 10 mg/kWh, respectively [14-16] and the national standard GB 20891-2014 for non-road Diesel engines requires that PM emission limits reach 0.025g/kWh in China [17]. Thus, the soot removal technology has become an important topic on improving environment level and protecting human

health. The use of Diesel particulate filter (DPF), which is placed downstream of Diesel oxidation catalyst (DOC), has been proven to be an effective way to remove Diesel PM emissions [1,18-22]. Its function is to capture PM through a wall-flow filtration mechanism. However, the saturated accumulation of PM in DPF can cause higher backpressure that has many negative impacts on engine working, thus DPF has to be regenerated by PM combustion [1]. The active or passive regeneration of DPF is crucial in controlling soot emission. The soot particulates are oxidized periodically by O_2 at higher temperatures (> 550 °C) during active regeneration and also oxidized continuously over the catalysts mainly by NO_2 during passive regeneration [7,23-27]. The regeneration efficiency strongly depends on the reactivity of soot, the burning of high-activity soot occurs at lower temperatures with small energy demand, for example low fuel consumption [1,7]. Many studies also confirmed that the reactivity of soot is related to soot nanostructure [28,29], soot morphology [28,30], fuel types [29,31,32], catalyst materials [23-27,33] and engine operation conditions [34,35].

Carbon is the main composition (> 80 wt.%) of Diesel soot with a small amount of soluble organic fraction (SOF) and ash [36-38]. The formation of Diesel soot particulates must experience nucleation, nanoparticles aggregation and surface growth steps, accompanied by the evolution of their structure [38,39]. The primary carbon particles are composed of ordered and amorphous carbons. The ordered carbon surface shows a graphite-like structure with higher crystalline order and the amorphous carbon presents lower degree of graphitization with many active edge sites and defects [40-44]. The different structural features of soot particles would determine their physicochemical properties and thereby their reactivity [41-46].

Boehman et al. [47] reported that the disordered carbon with more amorphous structure had more defects and thus exhibited higher reactivity. Many authors also studied the relationship between soot structure and reactivity by Raman microspectroscopy and high-resolution transmission electron microscopy (HRTEM) [28,43,44,48]. It was found that the higher reactivity of soot was attributed to a higher degree of disorder and a higher content of molecular carbon, which is because higher amount of defects in carbon structure results in an increase in surface functionalization [28]. It was also reported that the reactivity of soot would be

dependent on its primary particle size characterized by TEM [29,48]. On the other side, some researchers found that the presence of oxygenated additives in fuels enhanced the formation of oxygenated soot and thereby increased the oxidative reactivity of soot [31,43,44,48-50]. This might be ascribed to higher content of oxygen in soot particles produced from oxygenated fuel combustion [31,50,51]. Therefore, the use of Biodiesel fuel as oxygenated fuel can apparently improve non-catalytic and catalytic reactivity of soot [31,44,48,52].

Besides, the catalytic materials coated on the DPF wall also play an important role on determining the catalytic oxidation reactivity of Diesel soot since they are able to decrease soot oxidation temperature. A large number of publications reveal a wide study of catalyst materials used for DPF regeneration, which include noble metal catalysts [23,24,53], perovskite-type catalysts [54,55], and ceria-based catalysts [56-61]. Among them, the latter are more desirable catalyst materials for DPF regeneration than the former two due to their lower cost and higher oxygen storage/release capacity. It was reported that ceria-based mixed oxides can generate a great quantity of active oxygen species (e.g. O^-, O_2^-, O_2^{2-}), resulting from many oxygen vacancies and high mobility of oxygen, and thus exhibit higher catalytic activity for soot oxidation [26,57-64]. In addition, a higher oxidizing ability of NO into NO_2 over ceria-based catalysts is also an advantage in promoting DPF passive regeneration [27,58,68-70].

In Knauer's work [28], the authors prepared the oxidized/activated Diesel soot samples through Temperature-Programmed Oxidation (TPO) method in a temperature range from 25 to 600 °C under O_2 and studied the differences in nanostructure between raw and oxidized soot samples. They found that the changes in chemical homogeneity and structural order of Diesel soot occurred after partial soot oxidation. In real exhaust aftertreatment system, soot particles which are generated from Diesel engine follow thermal gas-flow line and go through Diesel Oxidation Catalyst (DOC) unit, and then are accumulated and regenerated in DPF [22,71]. In this process, Diesel soot would be partially oxidized or activated before its complete combustion. It may result in an impact of soot structure and even soot oxidation reactivity. However, this point is hardly noticed in the previous studies.

Thus, the present work aims to investigate the influence of soot activation on non-catalytic and catalytic reactivity, determined by Temperature-programmed Oxidation (TPO) tests, and structural and surface properties, characterized by BET, Raman spectra, HRTEM, Diffuse Reflectance Infrared Fourier Transform Spectra (DRIFTS) and XPS. The real Biodiesel and Biodiesel-Diesel blend soot samples generated on a real Diesel engine bench were used in this work. Printex U (Degussa) as a model soot has been widely used for experimental work. So its activation was also studied and compared with real Bio soot.

2. Experimental

2.1. Materials preparation

2.1.1. Soot samples preparation

The oxidized/activated soot samples were prepared by Temperature Programmed Oxidation (TPO) method under 9% b.v. O_2/Ar (250 ml/min). A carbon black (Printex-U) from Degussa as representative of model soot and Biodiesel derived soot B7 and B100, which separately generated from the burning of 7% Biodiesel-Diesel blends and 100% Biodiesel in a real Diesel engine [48], were used for this study. As shown in Fig. 1, when soot-TPO was performed till 500 °C (about 3-10% conversion) and 600 °C (about 20-30% conversion), respectively, the activated soot samples were taken out from the reactor and marked "soot-500" and "soot-600". The raw soot samples were used as a reference.

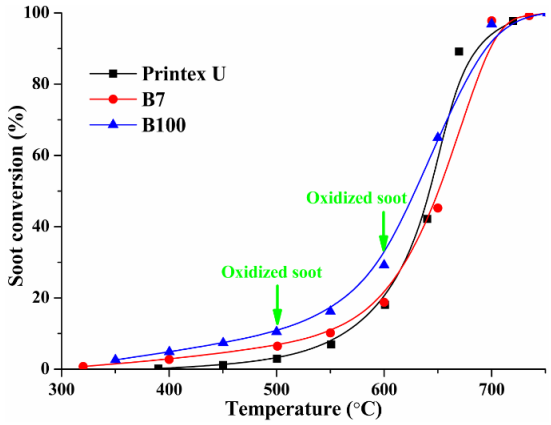

Fig. 1. Soot conversion in TPO under 9% b.v. O_2/Ar at a heating rate of 10 °C/min.

2.1.2. Catalyst preparation

MnO_x-CeO_2 mixed oxides (CM) (Mn/Ce = 1/4 (mol/mol)) were prepared through a

co-precipitation method and used to evaluate the catalytic activity of soot. $Ce(NO_3)_3 \cdot 6H_2O$ (solid, 95% pure) and $Mn(NO_3)_2$ (liquid, 50 wt.%) as the precursors were firstly dissolved in deionized water, then the mixture solution was mixed with the precipitant (pH > 9.0) consisting of $NH_3 \cdot H_2O$ and $(NH_4)_2CO_3$ (chemical reagents, Beijing). The obtained precipitates were filtered and dried by a spraying apparatus, then calcined in static air at 500 °C for 3 h in a muffle furnace.

2.2. Soot characterization

The particles size distribution of soot was measured on FRITSCH laser particle sizer (ANALYSETTE 22 Nano Tec). Prior to each measurement, the aggregated soot sample was well dispersed in water by a close circulatory system and an integrated ultrasonic generator.

The special surface area of soot samples was measured on an automatic surface analyzer by N_2 adsorption/desorption method at -196 °C. Prior to tests, the samples were degassed at 200 °C for 2 h under vacuum.

Raman spectra of soot were obtained on an inVia Reflex spectrometer (Renishaw, London, England) with a YAG laser (532 nm). The output power of 0.9 mW was chosen in the scanning range of 800-3500 cm^{-1}. The spectrometer includes a grating with 600 grooves mm^{-1} and a CCD detector with ×50 magnification objective lens.

The morphology of soot was analyzed by high-resolution transmission electron microscopy (HR-TEM) (Tecnai G^2 F20) with an acceleration voltage of 200 kV. The soot powders were dispersed in ethanol and deposited over Cu grids with a holey carbon film.

XPS measurement was conducted on an AXIS Ultra DLD spectrometer (Kratos, England) by using AlKα radiation as the excitation source (300 W). All binding energies (B.E.) were referenced to carbon C 1s line at 284.6 eV.

DRIFTS (diffuse reflectance infrared Fourier transform spectra) of soot were measured by using a Nicolet 6700 spectrometer with a DTGS detector and a high temperature cell. Soot sample was diluted by KBr at a soot/KBr ratio of 1/40, then the mixture was placed in a reaction cell and pretreated at 100 °C in pure N_2 for 10 min. After that, the IR spectra were recorded.

181 *2.3. Reactivity measurement*

182 The reactivity of soot samples was measured by temperature-programmed
183 oxidation (TPO) under 9% b.v. O_2/Ar and 400 ppmv NO + 9% b.v. O_2/Ar. Prior to the
184 catalytic reactivity measurement, soot and the catalyst powder were mixed by a loose
185 contact at a weight ratio of 1/10 (2.0 mg/20 mg). To minimize the impact of hot spots,
186 the soot-catalyst mixture (22 mg) was diluted with 80 mg SiC pellets. The final
187 mixture was heated in a U-shaped quartz reactor at a ramp rate of 10 °C. The flow rate
188 was controlled to 250 ml/min (15 Nl/h). 2 mg soot and 80 mg SiC pellets were mixed
189 and then used for non-catalytic reactivity measurement under 9% b.v. O_2/Ar.
190 Concentrations of CO and CO_2 (ppmv) were recorded by a Siemens Ultramat6
191 analyzer. In the obtained soot-TPO curves, T_i and T_m represent the ignition
192 temperature at which the CO_x (CO + CO_2) concentration reaches 100 ppm and the
193 temperature of maximal soot oxidation rate, respectively.

194 Based on the reaction C(soot) + (1 + x)/2O_2 → $x$$CO_2$ + (1-x)CO, the specific
195 reaction rate (V_{spec}) was normalized to catalyst quality (20 mg) or soot mass (2 mg)
196 and thus calculated by the following equation:

197

198 $$V_{spec} = \frac{(X_{CO} + X_{CO2}) \times D}{3600 \times V_M \times m_{cat.}} \qquad \text{(a)}$$

199 or

200 $$V_{spec} = \frac{(X_{CO} + X_{CO2}) \times D \times 10^{-3}}{3600 \times V_M \times m_{ini.}} \qquad \text{(b)}$$

201

202 Where V_{spec}: the specific reaction rate in (a) $\mu mol_{soot}/s/g_{cat.}$ or (b) $mmol_{soot}/s/g_{ini.}$,
203 X_{CO} and X_{CO2}: molar fractions of CO and CO_2 in ppmv,
204 D: flow rate (15 Nl/h),
205 V_M: molar volume (22.4 L/mol),
206 $m_{cat.}$: mass of catalyst (0.02 g),
207 $m_{ini.}$: mass of initial soot (0.002 g)

208 *2.4. Isothermal experiment*

209 Isothermal experiments of soot oxidation were conducted at 350 °C under 9% b.v.
210 O_2/Ar and 400 ppm NO/9% b.v. O_2/Ar, respectively, to obtain the specific reaction

rate of soot. There is no apparent increase in soot conversion at 350 °C, thus soot oxidation reaction is in a relatively stable state. High space velocity and mixing SiC powder effectively inhibit the mass and heat transfer, and thereby soot oxidation reaction can be mostly controlled by the chemical kinetics [67,68]. After isothermal reaction for 1800 s, the "initial soot oxidation rate" at the starting of isothermal reaction and the "final soot oxidation rate" at the end were thus recorded.

3. Results and discussion

3.1. Reactivity analysis

3.1.1. TPOs in O_2

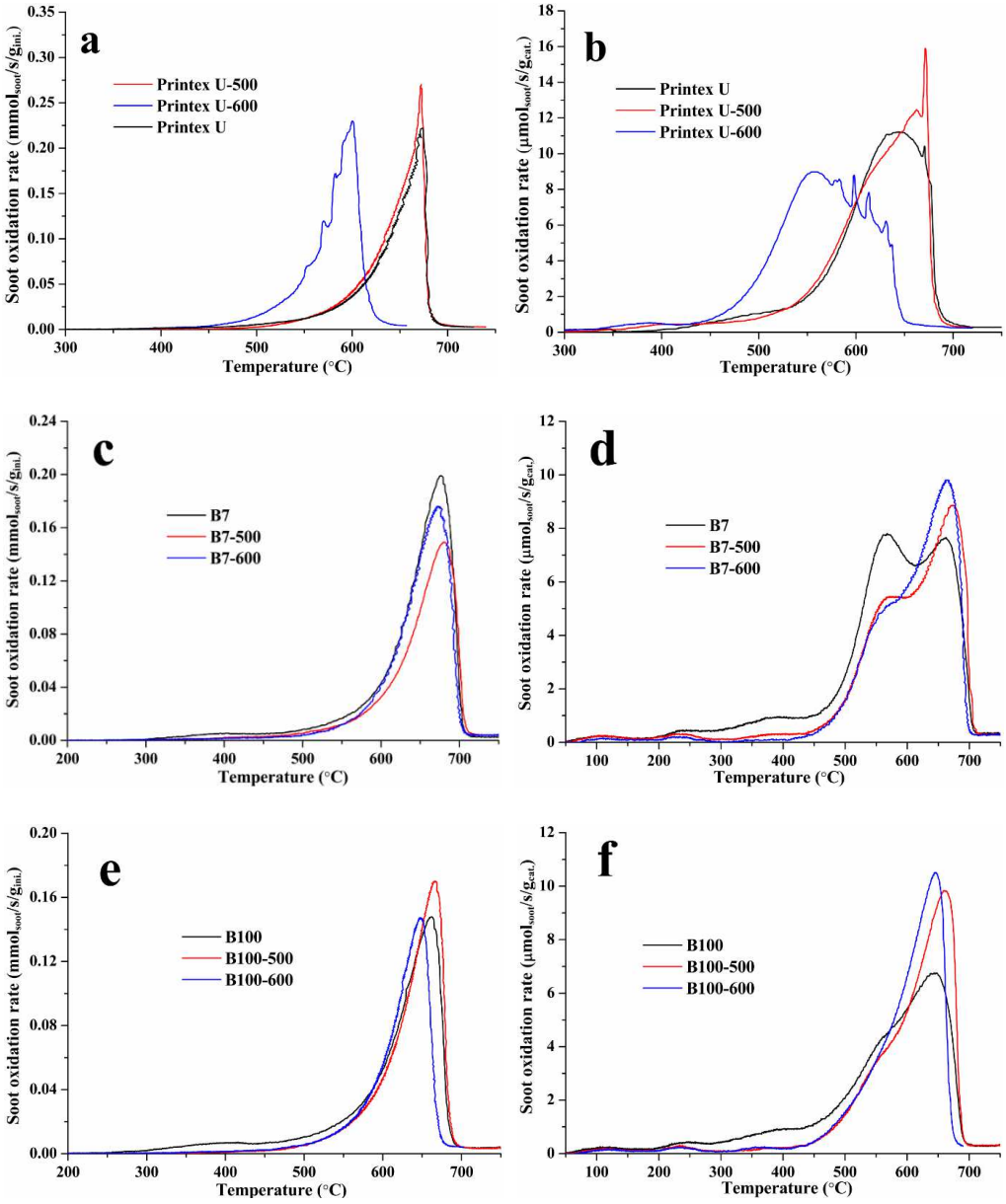

Fig. 2. Non-catalytic (a, c, e) and catalytic (b, d, f) reactivities of raw and oxidized soot samples

under 9% b.v. O_2/Ar. Reaction conditions: soot mass is 2.0 mg, catalyst mass is 20.0 mg, 80 mg SiC was used for dilution, the flow rate is 250 ml/min, heating rate is 10 °C/min.

Table 1. T_i and T_m values of TPOs with different soot samples.

Samples	In O_2		In NO + O_2	
	T_i/°C	T_m/°C	T_i/°C	T_m/°C
Printex U	535[a]/483[b]	674[a]/644[b]	412[b]	609[b]
Printex U-500	540/508	672/662	382	580
Printex U-600	484/458	600/560	338	490
B7	511/379	676/662	370	556
B7-500	534/479	681/673	378	553
B7-600	540/483	672/664	374	543
B100	490/414	662/644	339	565
B100-500	527/480	667/662	404	590
B100-600	528/477	647/646	382	561

[a]The values were obtained without catalyst.

[b]The values were obtained with catalyst.

To explore the impact of thermal activation or partial oxidation of soot on its reactivity, the TPO experiments of raw and activated soot samples were conducted in 9% b.v. O_2/Ar. Fig. 2a shows the non-catalytic activities of the raw and activated Printex U samples. By comparison, the activated soot Printex U-600 (about 20% of conversion) presents an apparently increased reactivity, its T_i and T_m values visibly decrease to 484 and 600 °C from 535 and 674 °C of raw soot, respectively (Table 1). However, the activated soot Printex U-500 (about 3% of conversion) has no apparent changes in reactivity compared to raw soot. Table 1 also lists their similar T_i and T_m values. Fig. 2b presents the catalytic activities of Printex U samples. The same phenomenon can be observed that the conversion temperatures of Printex U-600 visibly shift towards lower values compared with that of raw soot, for example, the T_i and T_m separately shift to 458 and 560 °C from 483 and 644 °C (Table 1). While the TPO curve of Printex U-500 seems to be similar with that of raw soot and shows a slight increase in T_i and T_m values. These results illustrate that the Printex U-600 is more reactive than Printex U-500 and raw Printex U.

The Bio soot B7 and B100 were produced on a real engine bench using a medium duty Diesel engine. Their non-catalytic and catalytic activities were also tested by TPO before and after activation and the results are shown in Fig. 2c-f. It can be seen

247 that for the activated B7 and B100 samples, the low-temperature reactivity decreases
248 compared to raw soot. Table 1 also illustrates that the T_i values of the activated B7
249 and B100 samples are higher than those of raw soot during both non-catalytic and
250 catalytic oxidation. Besides, T_m values of B7-600 and B100-600 are similar with those
251 of raw soot and do not visibly shift to lower temperatures (except for non-catalytic
252 reactivity of B100-600). It is also observed that the T_m of B7-500 and B100-500
253 slightly shifts to higher temperatures compared to that of raw samples. Thus, the
254 partial oxidation process of real Bio soot decreases the low-temperature reactivity (T_i)
255 but cannot apparently affect the high-temperature reactivity (T_m). These results are
256 contrary to those of Printex U samples.
257

258

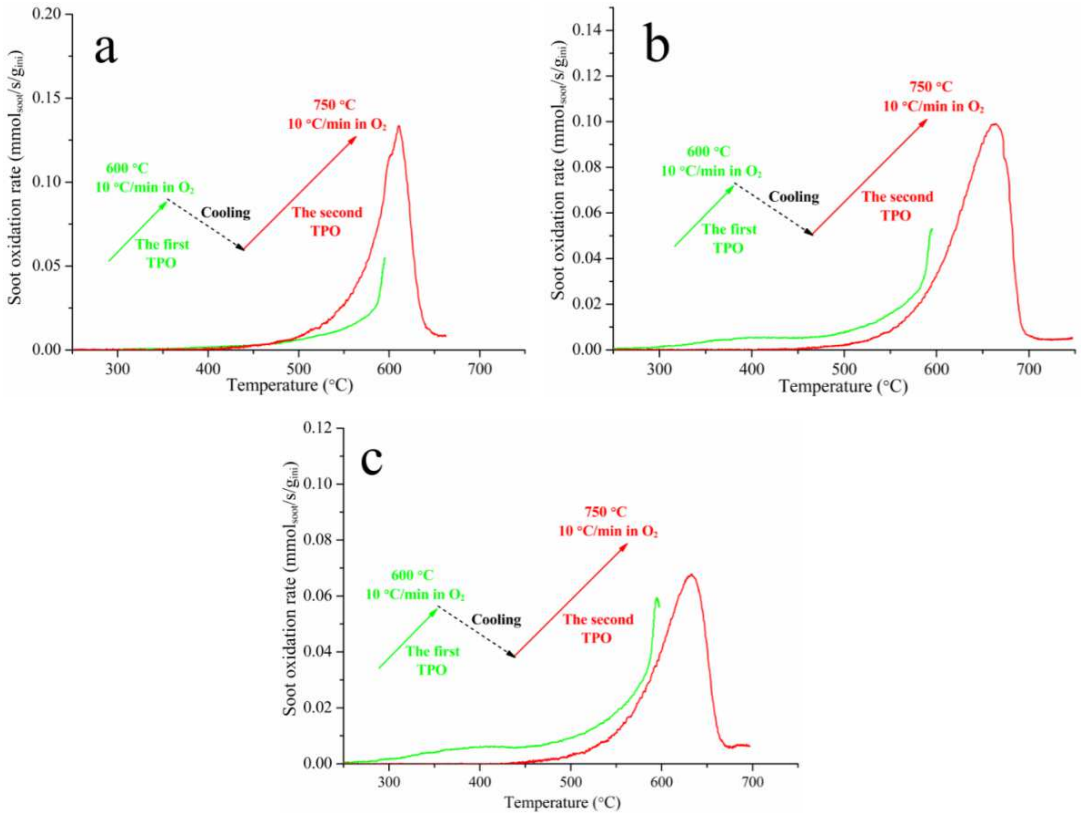

259

260 **Fig. 3.** The first and second TPO profiles of raw Printex U (a), B7 (b) and B100 (c) samples.
261 Experimental conditions: soot mass is 2.0 mg, SiC mass is 80 mg, without catalyst, the flow rate is
262 250 ml/min, heating rate is 10 °C/min.

263 To confirm the influence of the activation step on the reactivity of soot, firstly, the
264 raw soot samples were partially oxidized under O_2/Ar through TPO step from 25 to
265 600 °C, then the activated soot was cooled down to 25 °C and the second TPO was

performed to obtain the total soot conversion profile. As shown in Fig. 3, for Printex U soot (Fig. 3a), the soot oxidation temperatures for the second TPO curve visibly shift to lower values relative to the first TPO, which reveals a promoting role of the activation step on soot oxidation. For B7 and B100 samples (Fig. 3b, c), it can be clearly observed that the second TPO profile presents a decreased reactivity (< 600 °C) compared with the first TPO. These results above are in good agreement with those presented in Fig. 2.

3.1.2. TPOs in NO + O_2

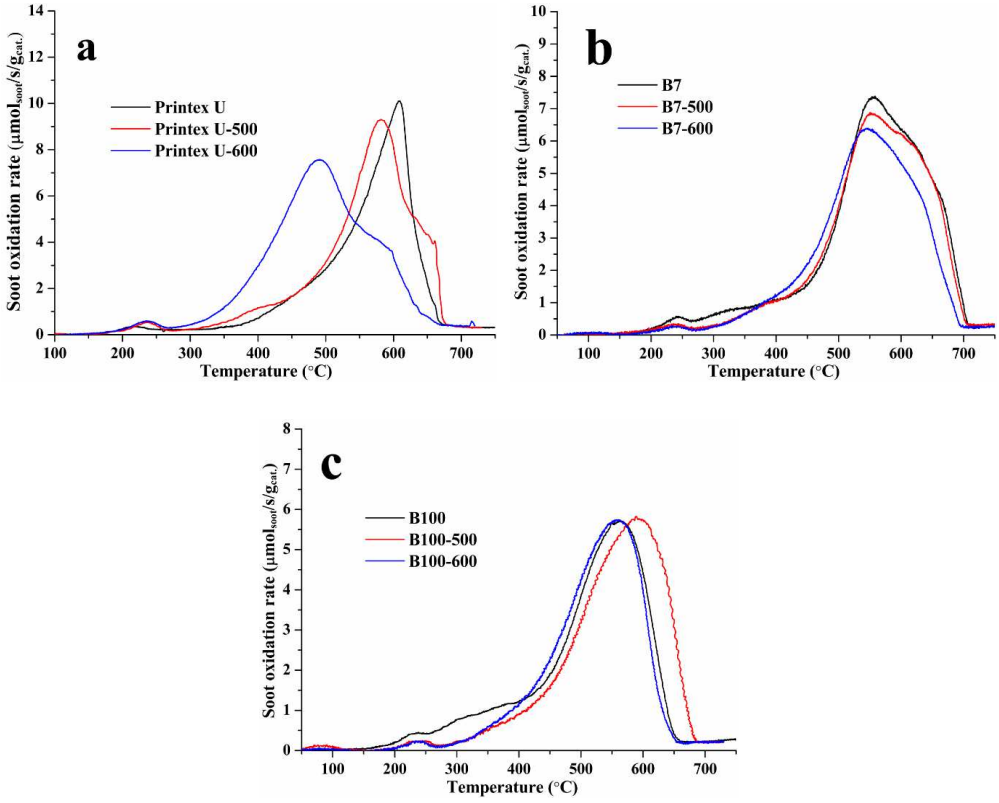

Fig. 4. Catalytic reactivities of Printex U (a), B7 (b) and B100 (c) samples under 400 ppm NO + 9% O_2/Ar. Reaction conditions: soot mass is 2.0 mg, catalyst mass is 20.0 mg, soot and catalyst were mixed by loose contact and then diluted by 80 mg SiC, the flow rate is 250 ml/min, heating rate is 10 °C/min.

It was reported that the presence of NO can promote the oxidation of soot over Mn-Ce catalysts, which is ascribed to two factors: firstly, NO is able to be oxidized into NO_2 with higher oxidizing ability than O_2 over Mn-Ce mixed oxides [58,68]; secondly, the adsorption/desorption of NO on Mn-Ce mixed oxides can increase oxygen vacancies and desorption of active oxygen [69]. In the present work, TPO profiles of the catalytic oxidation of Printex U and Bio soot samples under 400 ppm

NO + 9% b.v. O_2/Ar are presented in Fig. 4. An apparent promotion of NO on soot activity can be observed by comparing the TPO profiles in Fig. 4 and Fig. 2. In the case of Printex U, in comparison with raw soot, the oxidized samples especially for Printex U-600 show an increased reactivity. It can be noted in Table 1 that the T_i and T_m of Printex U-500 slightly shift to lower values but those of Printex U-600 display a larger shift. In the previous TPO with catalyst under O_2 (Fig. 2b), Printex U-500 presents a similar TPO curve with the raw soot, and the T_i and T_m of Printex U-600 decrease by 25 and 84 °C, respectively, relative to those of raw Printex U. However, in NO + O_2 (Fig. 4a), Printex U-500 exhibits a slight enhancement on soot oxidation activity and the T_i and T_m of Printex U-600 separately decrease by 74 and 119 °C compared to those of raw soot. The fact illustrates that the reactivity of the activated Printex U soot is more easily promoted in NO + O_2. In the case of B7 and B100, it can be clearly observed that the low-temperature reactivity of activated soot samples decreases at about 200-350 °C. The results are also confirmed in Fig. 2. For B7 soot, the high-temperature reactivities of raw B7 and B7-500 samples are almost similar in view of the close T_m values (556 and 553 °C), and that of B7-600 shows a slight promotion. For B100 soot, the T_m value of B100-500 shifts towards higher temperature (590 °C) and that of B100-600 (561 °C) is similar compared with raw soot (565 °C).

3.1.3. Isothermal reaction rate at 350 °C

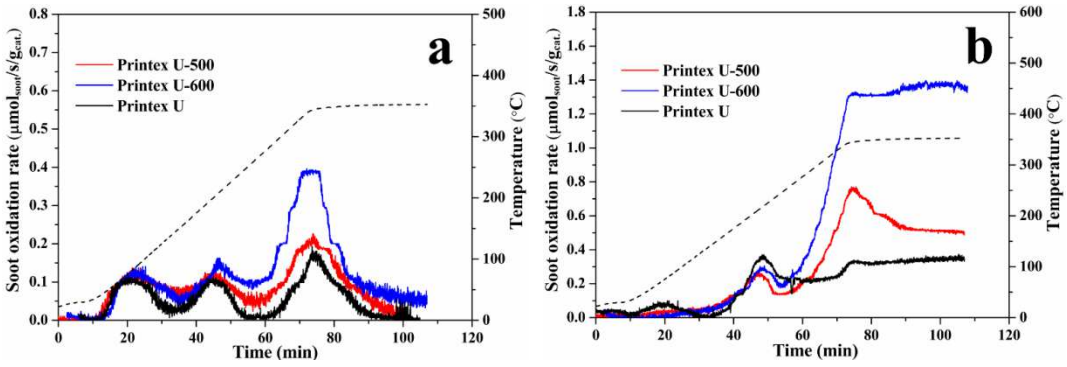

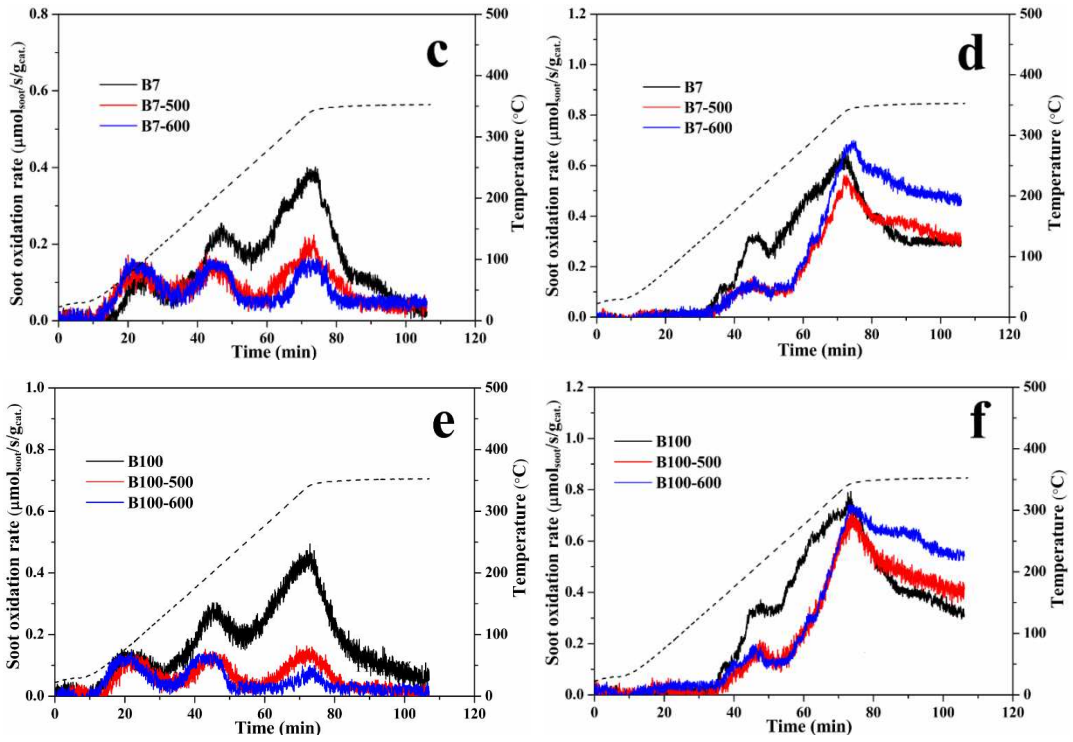

Fig. 5. Isothermal catalytic reaction at 350 °C in 9% O_2/Ar (a, c, e) and 400 ppm NO + 9% O_2/Ar (b, d, f). 2 mg soot and 20.0 mg catalyst were mixed by loose contact, 80 mg SiC pellets were used for dilution, the flow rate is 250 ml/min.

Table 3. The results of isothermal reaction at 350 °C.

Soot sample	9% O_2		400 ppm NO + 9% O_2	
	Initial oxidation rate ($\mu mol_{soot}/s/g_{cat.}$)	Final oxidation rate ($\mu mol_{soot}/s/g_{cat.}$)	Initial oxidation rate ($\mu mol_{soot}/s/g_{cat.}$)	Final oxidation rate ($\mu mol_{soot}/s/g_{cat.}$)
Printex U	0.1791	0.0082	0.3291	0.3484
Printex U-500	0.2156	0.0082	0.7614	0.5066
Printex U-600	0.3922	0.0538	1.3092	1.3532
B7	0.3928	0.0251	0.6409	0.3055
B7-500	0.2011	0.0433	0.5450	0.3146
B7-600	0.1524	0.0480	0.6774	0.4604
B100	0.4612	0.0814	0.7631	0.3238
B100-500	0.1492	0.0243	0.7312	0.4077
B100-600	0.0884	0.0243	0.6855	0.5471

Fig. 5 and Table 3 show the catalytic reaction rates of raw and activated soot samples under isothermal conditions. As shown in Fig. 5a and Fig. 5b, the catalytic reaction rates of raw and activated Printex U samples follow the order Printex U-600 > Printex U-500 > Printex U at 350 °C in both O_2 and NO + O_2. This reveals

that the activated Printex U shows higher reactivity for soot oxidation. Especially in the presence of NO, a more apparent increase in the reaction rate of the activated samples is observed in Fig. 5b and Table 3.

It is interesting to undernote that, not all soot samples can show the same phenomenon with Printex U after activation. As shown in Fig. 5c-f and Table 3, for real soot B7 and B100, the activated soot samples exhibit decreased oxidation rates in O_2 but increased results in NO + O_2. In Table 3, it can be observed that the initial oxidation rates of the activated B7 and B100 samples visibly decrease in O_2. A slight increase in final oxidation rates of the activated B7 samples can be also seen, but the oxidation rates are too small to illustrate the real case. In the case of the TPO results in NO + O_2, the initial oxidation rates of B7 and B100 samples are ranked as follow: B7-600 (0.6774 $\mu mol_{soot}/s/g_{cat}$) > B7 (0.6409 $\mu mol_{soot}/s/g_{cat.}$) > B7-500 (0.5450 $\mu mol_{soot}/s/g_{cat.}$) and B100 (0.7631 $\mu mol_{soot}/s/g_{cat.}$) > B100-500 (0.7312 $\mu mol_{soot}/s/g_{cat.}$) > B100-600 (0.6855 $\mu mol_{soot}/s/g_{cat.}$), respectively. However, their final oxidation rates apparently increase after soot activation (Table 3). In previous TPO results, it can be noted that the activated B7 and B100 samples show a decreased low-temperature catalytic reactivity in both O_2 and NO + O_2 mixture. The results in isothermal reactions under O_2 (Fig. 5c, e) are in good agreement with this point, but those in NO + O_2 (Fig. 5d, f) exhibit a contrary result. The fact illustrates that under isothermal conditions the presence of NO is more favorable for the catalytic oxidation of activated Bio soot.

Moreover, it can be noticed that for the isothermal reactions under O_2 the final reaction rates sharply decline relative to the initial ones, but the presence of NO into O_2 apparently inhibits the decrease of reaction rates and makes the final reaction rates remain higher values. The result would be attributed to the following reasons: (1) MnO_x-CeO_2 mixed oxides have higher catalytic oxidation activity of NO into NO_2 [57,58,69], the produced NO_2 with stronger oxidizing ability than O_2 can enhance the soot oxidation rate; (2) the production of NO_2 over MnO_x-CeO_2 catalyst benefits C + NO_2 + O_2 cooperative reactions [58,70]; (3) it was confirmed that NO adsorption/desorption on MnO_x-CeO_2 enhances the production of active oxygen in the oxides [69].

In Seong's work [72], the authors analyzed the burning process of soot through partially oxidizing Printex-U soot under O_2-NO_2 mixtures and found that the oxidation-derived maturing process was much dependent on NO_2 content. Besides, the presence of NO_2 during soot oxidation has been confirmed to have a good promoting role on the oxidative reactivity of soot [23,24,58,64,72]. Thus, we suppose that the activation of soot under different reaction gases would cause different oxidation reactivities of the activated soot. In the present work, Printex U soot was chosen and partially oxidized by TPO from 25 to 500 °C in 9% O_2/Ar, 400 ppm NO + 9% O_2/Ar and 400 ppm NO_2 + 9% O_2/Ar, respectively. Then these activated soot samples were used for isothermal catalytic reactions under NO + O_2 at 350 °C to compare their differences. As presented in Fig. S1 (see Supplementary Materials), the isothermal reaction curves of the activated soot samples seem to have no more apparent differences. When the reaction rate reaches a stabilized value, it can be clearly seen that the activated soot under NO + O_2 shows a similar oxidation rate (about 0.51 $\mu mol_{soot}/s/g_{cat.}$) compared to that one under O_2, but under NO_2 + O_2 a slightly increased oxidation rate (about 0.57 $\mu mol_{soot}/s/g_{cat.}$). This might be because the presence of NO_2 affects the structure of soot particles and thereby the oxidation reactivity during the activation process [34,72].

3.2. *Soot characterization*

3.2.1. Laser granulometry

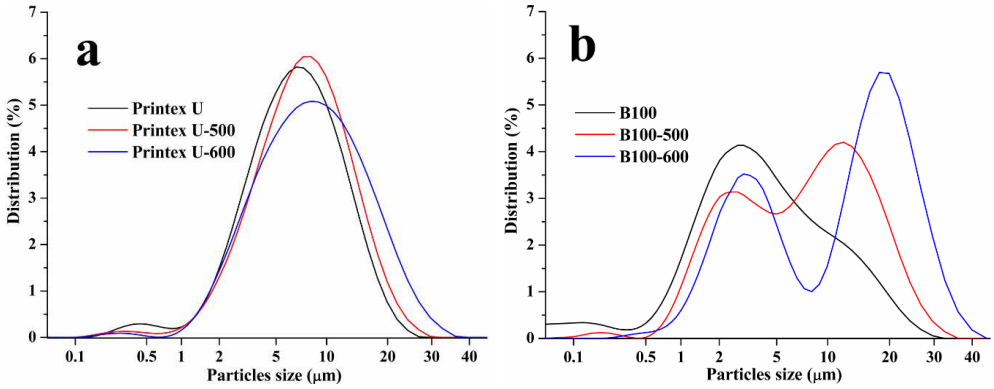

Fig. 6. Particles aggregates size distribution of Printex U (a) and B100 (b) samples.

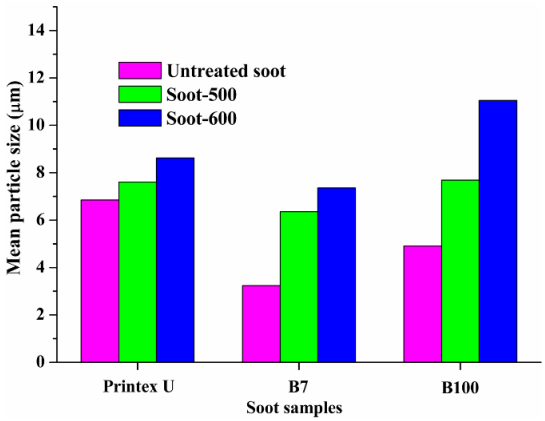

372

373 **Fig. 7.** Mean size of particles aggregates of different soot samples.

374 Fig. 6 presents the size distributions of particles aggregates of raw and activated
375 Printex U and B100 samples. It can be clearly seen that the activated soot samples
376 show different size distribution profiles compared to raw soot. For the two soot
377 samples Printex U and B100, it is found that the activation step leads to a decrease in
378 the amount of smaller soot particles and the whole distribution profiles of activated
379 soot shift towards higher values. The same result can be also observed for the raw and
380 activated B7 soot samples (Fig. S2, see the Supplementary Materials). As shown in
381 Fig. 7, the mean size of soot particles aggregates increases after the activation, with
382 following the order: raw soot < soot-500 < soot-600. Especially for the real soot B7
383 and B100, the activated soot samples exhibit a larger increase in particles aggregates
384 sizes than Printex U. These results also illustrate that the soot particles with smaller
385 aggregates sizes would be firstly oxidized during soot oxidation.

386

387 *3.2.2. BET test*

388 **Table. 4.** Textual properties of raw and activated soot samples

Soot sample	S_{BET} (m^2/g)[a]	Mean pore size R (nm)[a]	Pore volume V_p (ml/g)[a]
Printex U	97.8	18.94	0.90
Printex U-500	111.8	19.07	1.05
Printex U-600	321.3	1.21	1.30
B100	124.1	39.01	1.26
B100-500	154.9	1.64	0.92
B100-600	217.1	1.21	1.29
B7	231.6	25.55	2.73
B7-600	296.2	1.21	1.91

[a]which was calculated by BJH method.

Table 4 lists the values of special surface area (S_{BET}), mean pore size (R) and pore volume (V_p) of the raw and activated soot samples. The activation of raw soot significantly increases the surface area and decreases the mean pore size. This illustrates that the activation process results in a modification of textural property of soot. For Printex U samples, Printex U-500 shows a slight increase in S_{BET} and R, while Printex U-600 has a sharp increase in S_{BET} and a decrease in R. The pore volume (V_p) of Printex U also exhibits an increased trend after the activation. For real Bio soot B7 and B100, a similar change in S_{BET} and R with Printex U can be observed after activation, but one different point is that V_p values of B7-600 and B100-500 decrease compared to raw soot. The sharp decrease of mean pore size for the activated soot indicates an apparent increase in the amount of smaller pores and a disappearance of large pores. It is speculated that the initial soot oxidation may occur in larger pores.

3.2.3. Raman analysis

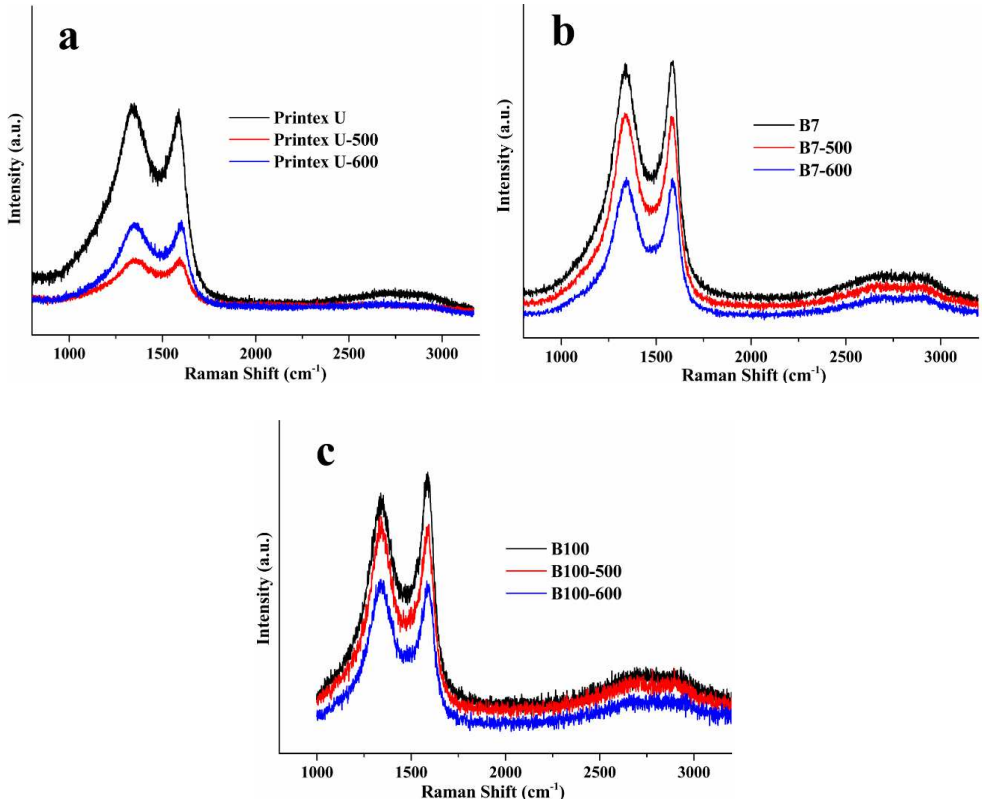

Fig. 8. Raman spectra of raw and partially oxidized Printex U (a), B7 (b) and B100 (c) samples.

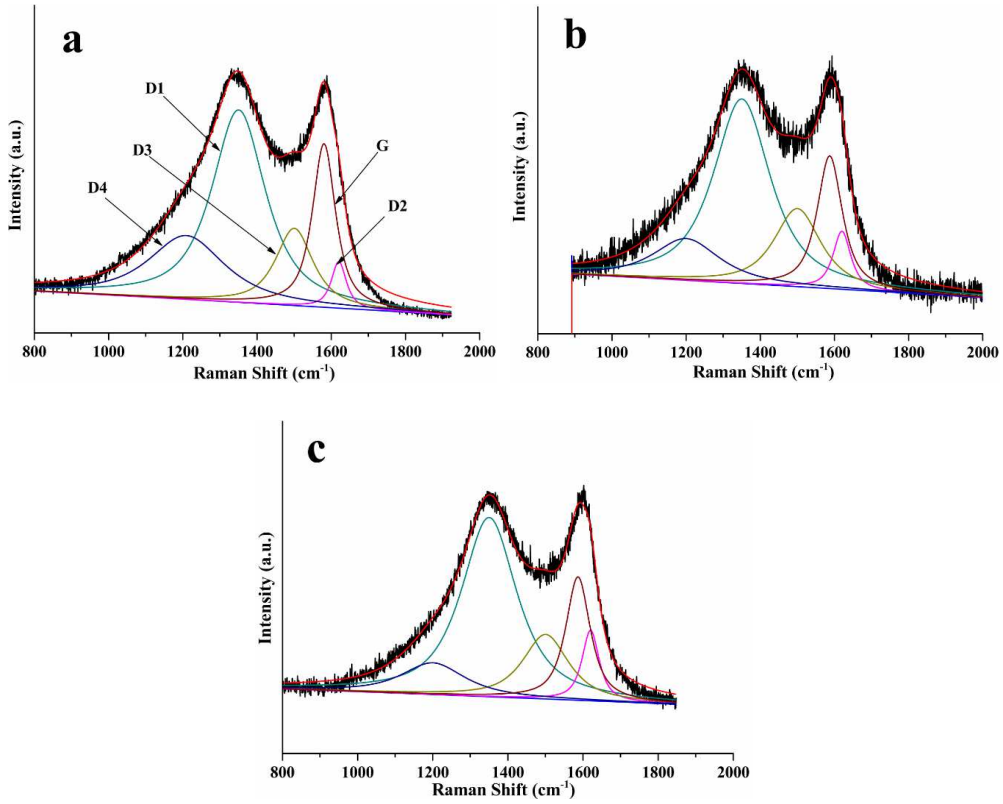

Fig. 9. Analysis of the Raman spectra and curve fits of raw Printex U (a), Printex U-500 (b) and Printex U-600 (c).

Table 5. Raman results of soot samples.

Sample	$FWHM_{D1}$/cm^{-1}	$FWHM_{D2}$/cm^{-1}	$FWHM_{G}$/cm^{-1}	I_{D1}/I_G	I_{D2}/I_G	I_{D3}/I_G	A_{D1}/A_G	A_{D3}/A_G
Printex U	174	47	70	1.04	0.87	0.90	2.7	0.75
Printex U-500	182	57	81	1.04	0.97	0.98	3.1	1.09
Printex U-600	179	51	81	1.03	0.97	0.97	3.3	0.97
B7	153	42	70	1.01	0.30	0.42	2.3	0.39
B7-500	149	39	67	1.07	0.37	0.44	2.6	0.44
B7-600	151	47	71	1.10	0.42	0.43	2.6	0.42
B100	154	37	61	0.98	0.38	0.47	2.3	0.42
B100-500	145	31	63	1.10	0.41	0.51	2.4	0.51
B100-600	166	31	65	1.09	0.34	0.49	2.4	0.56

The Raman spectra of raw and activated soot samples were measured to analyze the microstructural features and the results are presented in Figs. 8, 9 and Table 5. Fig. 9 presents the Raman analysis of Printex U samples, and that of B7 and B100 samples can be also found in Fig. S3 and Fig. S4 (see Supplementary Materials). The Raman spectra of these soot samples are characterized by two overlapping peaks, which appear at around 1580 cm^{-1} (G peak) and 1350 cm^{-1} (D peak), respectively [28,38,73]. The D peak is generally related to defect sites or disordered carbon and G peak involves the ordered carbon. As shown in Fig. 8, in comparison with untreated raw soot, which has more separated D and G peaks, the Raman spectra for activated samples show more strongly overlapping peaks. This might imply an increase in the content of molecular carbon in the activated soot [28]. Moreover, in Fig. 8, it is also observed that raw soot samples exhibit broad Raman signals in the range of about 2300-3200 cm^{-1}, these should be ascribed to second-order bands due to (2*D) overtones and (D + G) combinations of graphitic lattice vibration modes [38]. The second-order signals become less pronounced after activation treatment for Printex U soot (Fig. 8a), but the visible decrease in the second-order signals cannot be seen for the activated B7 and B100 soot (Fig. 8b and c). The result may illustrate that Printex U soot becomes more disordered than B7 and B100 soot after activation.

Fig. 9 clearly illustrates the Raman spectrum of soot consists of four Lorentzian-shaped bands (G, D1, D2, D4) at around 1580, 1350, 1620 and 1200 cm^{-1}, respectively, and a Gaussian-shaped band D3 at about 1500 cm^{-1} [28,73]. It has been reported that D1 band is associated with disordered graphitic lattice and D3 band is related to amorphous carbon or molecular carbon, thus D1 FWHM (full width at half maximum) and D3 band intensity as important parameters can provide some information about chemical structure of graphite-like and amorphous carbon [28,29]. Many earlier works have also reported the FWHM of G and D bands and the D/G band intensity ratios (I_D/I_G) can correlate with degree of graphitization of carbonaceous materials [74-79]. The authors thought that an increase in G and D band FWHM and I_D/I_G values indicates a decrease in order. It was also published that the ratios between D bands and G band areas (A_D/A_G) are related to the structural defects in graphene layers [29]. Since it is unclear which of these parameters should be used

for Raman analysis, most of parameters are used here for comparison.

Table 5 lists spectroscopic parameters of different soot samples. For Printex U soot, it is observed that the activated soot samples (Printex U-500 and -600) exhibit an increased spectroscopic parameters including D and G band FWHM, I_D/I_G and A_D/A_G. This result illustrates that the activated soot has higher disorder and more structural defects. Among these parameters, D1 band FWHM and A_{D1}/A_G values of the activated soot samples increase, but their I_{D1}/I_G values are very similar with that of raw soot. Here D1 FWHM should be more important parameter for analyzing carbon structure. The relative intensity of D3 band (I_{D3}/I_G) is associated with amorphous carbon or molecular carbon. The increase of I_{D3}/I_G value of the oxidized soot samples indicates an increase in molecular carbon. However, by comparison, the two activated Printex U samples (Printex U-500 and -600) show similar spectroscopic parameters, which seems to imply their similar structural features.

In the previous work [48], it has been proposed that the non-catalytic and catalytic reactivities of soot are correlated to their structural properties. In the present work, the previous TPOs results have confirmed that the activated Printex U samples show an improved reactivity compared to raw sample, this well agrees with the Raman results. Nonetheless, the similar Raman results of the two activated samples cannot explain much higher reactivity of Printex U-600 than the other one. This may illustrate that the reactivity of soot cannot be only ascribed to the structure but also to particle morphology [48,80], ash content and composition [81,82] as well as oxygen content [49].

On the other hand, in the case of real soot B7 and B100, it can be seen in Table 5 that they have different structural features after activation compared with model soot Printex U. For B7 soot, as listed in Table 5, the activated soot B7-500 shows slightly decreased FWHM values, which appears to imply an increase in order. However, the I_D/I_G and A_D/A_G exhibit increased values, this seems to reveal an inverse result. It has been reported that D band FWHM and I_D/I_G have no significant correlation with each other [38]. Thus, it is difficult to well analyze the nanostructure of soot by Raman measurement and it may need more evidences to illustrate the nanostructural features. For B7-600, D1 and G band FWHM values as well as I_{D3}/I_G ratio are very similar

with those of raw B7 sample. But other parameters especially for D2 band FWHM and I_{D2}/I_G exhibit an increased tend. It was reported that the I_{D2}/I_G ratio and the D2 band FWHM should be inversely proportional to the thickness of graphitic domains in soot [38,76]. Therefore, the increase in D2 band FWHM and I_{D2}/I_G might indicate the decrease of graphitic carbon.

For B100 soot, it can be seen in Table 5 that B100-500 sample shows apparently decreased D1 and D2 bands FWHM but increased G band FWHM, I_D/I_G and A_D/A_G values compared to raw soot. In general, the intensity of G band, D1 and G band FWHM as well as I_{D1}/I_G are related to the graphitic order. The decrease in D1 band FWHM seems to reveal an increase in graphitic order. However, the G band FWHM and I_{D1}/I_G increase, this inversely indicates a decrease in order. Additionally, I_{D3}/I_G as important parameter is often used to evaluate the amorphous carbon content of soot. The increase of I_{D3}/I_G implies an increase in amorphous carbon content. Plus the increased tend of A_{D1}/A_G and A_{D3}/A_G, these results may illustrate an increase in disorder for B100-500. In the case of B100-600, it can be observed in Table 5 that D1 and G band FWHM as well as A_{D3}/A_G exhibit higher values than both B100 and B100-500 samples, and I_{D1}/I_G, I_{D3}/I_G and A_{D1}/A_G show very close values with those of B100-500. The result illustrates B100-600 has a lower order compared to the raw and B100-500 samples.

3.2.4. HRTEM

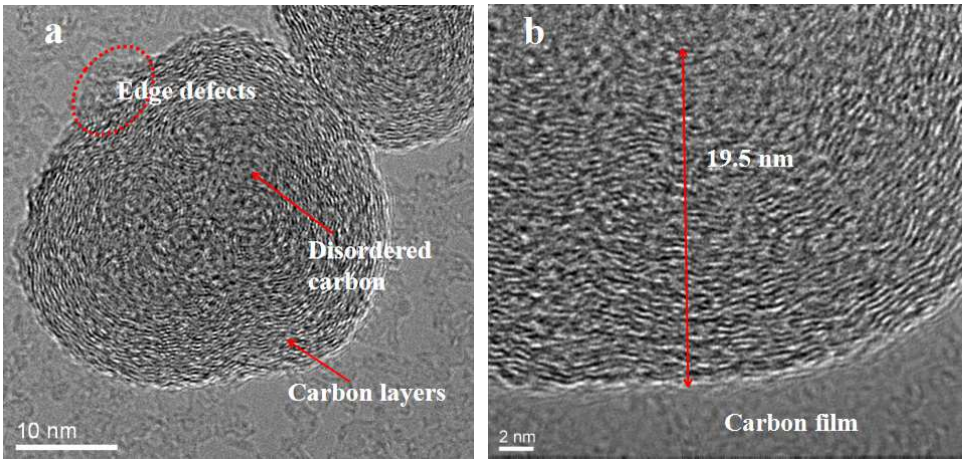

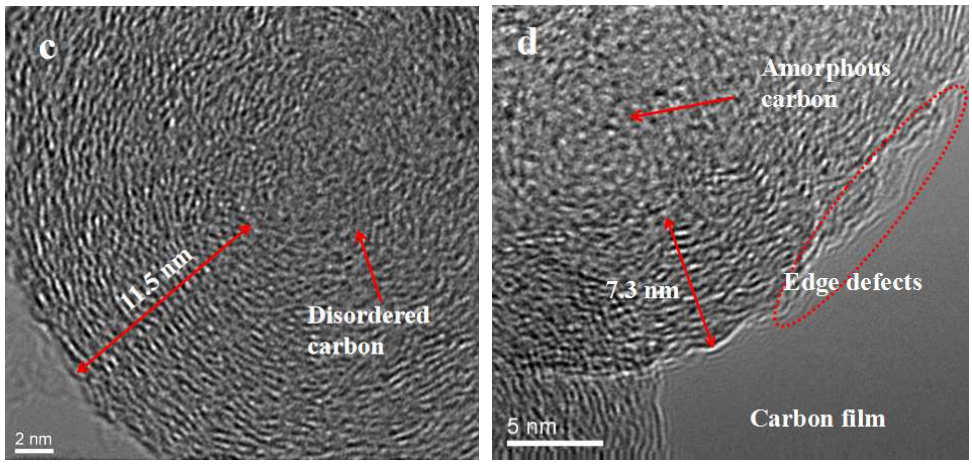

Fig. 10. HRTEM images of Printex U (a, b), Printex U-500 (c) and Printex U-600 (d).

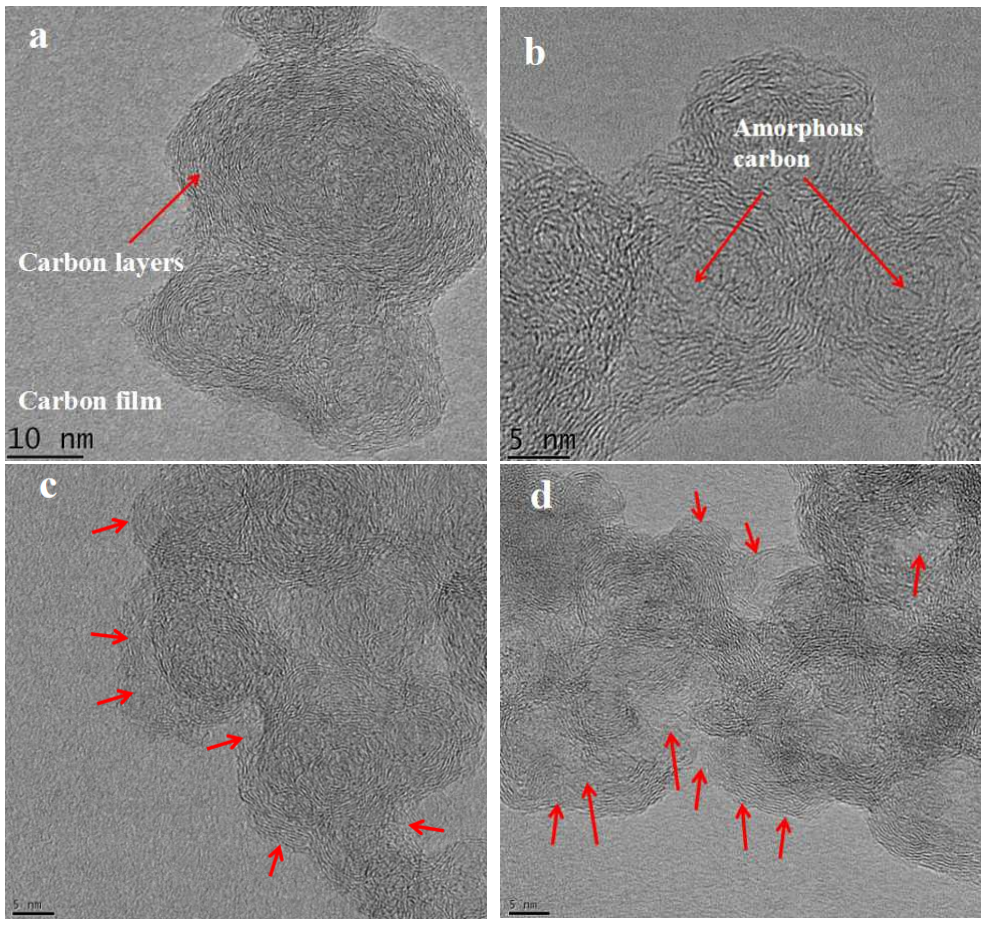

Fig. 11. HRTEM images of B100 (a, b), B100-500 (c) and B100-600 (d).

In order to better observe the structural and morphology changes of soot after activation, the morphology and nanostructural properties of Printex U and B100 soot samples were characterized by HRTEM, and the results are shown in Fig. 10 and Fig. 11. In the case of Printex U soot, as shown in Fig. 10a, it exhibits turbostratic patterns and an onion-like structure, the "tight" fringe layers concentrically surround nucleus

where the disordered carbon structure is observed. The raw Printex U also has a larger number of parallel stacked graphene layers with a larger thickness (about 19.5 nm) (Fig. 10b). This reveals a higher order for raw Printex U. Moreover, some edge defective sites are also observed in Fig. 10a. After the soot being activated, a decreased fringe-layer thickness can be clearly seen in Fig. 10c and d (about 11.5 nm for Printex U-500 and about 7.3 nm for Printex U-600). The result illustrates that the activation of Printex U decreases the degree of graphitization and Printex U-600 exhibits more apparent result. Besides, in comparison, it can be observed that the activated soot samples have an increased area of highly disordered carbon particles on the center. For example, for Printex U-600, the fringe patterns on the center become less noticeable, this is due to the oxidation of less-ordered nuclei through diffused oxygen into porous particles [83]. Thus, it is also confirmed that Printex U experienced an internal burning-out process during partial oxidation under O_2 [34,72].

The B100 Biodiesel soot exhibits different structural and morphology changes after activation compared with Printex U. As shown in Fig. 11a and b, the raw soot displays less obvious fringe layers and thinner carbon-layers thickness (about 5-10 nm) than raw Printex U soot. A less chainlike orientation and looser fringe layers are also observed in Fig. 11b. These results seem to illustrate that the real Bio soot has higher disorder and lower degree of graphitization than Printex U, which is also found in the previous work [48]. After partial oxidation, the activated samples B100-500 and B100-600 all show unclear fringe layers, especially for the edge area (red arrow). This might confirm that the activated samples become more disordered. In comparison in Fig. 11c, the edge of the B100-500 soot particle shows vaguer fringe layers than the area inside. Some void areas on the outer surface of primary particle are also found in Fig. 11d. Therefore, B100 soot tended to be oxidized through an external burning process during the activation [72].

Moreover, 50 soot particles were used for nanoparticles size analysis for each sample and nanoparticle-size distribution is presented in Fig. S5. With the soot being activated, the nanoparticles sizes of Printex U and B100 tend to decrease. Thus, the activated soot presents a smaller mean particle size than raw soot. This observation was also reported in Al-Ourashi's work [34].

3.2.5. XPS analysis

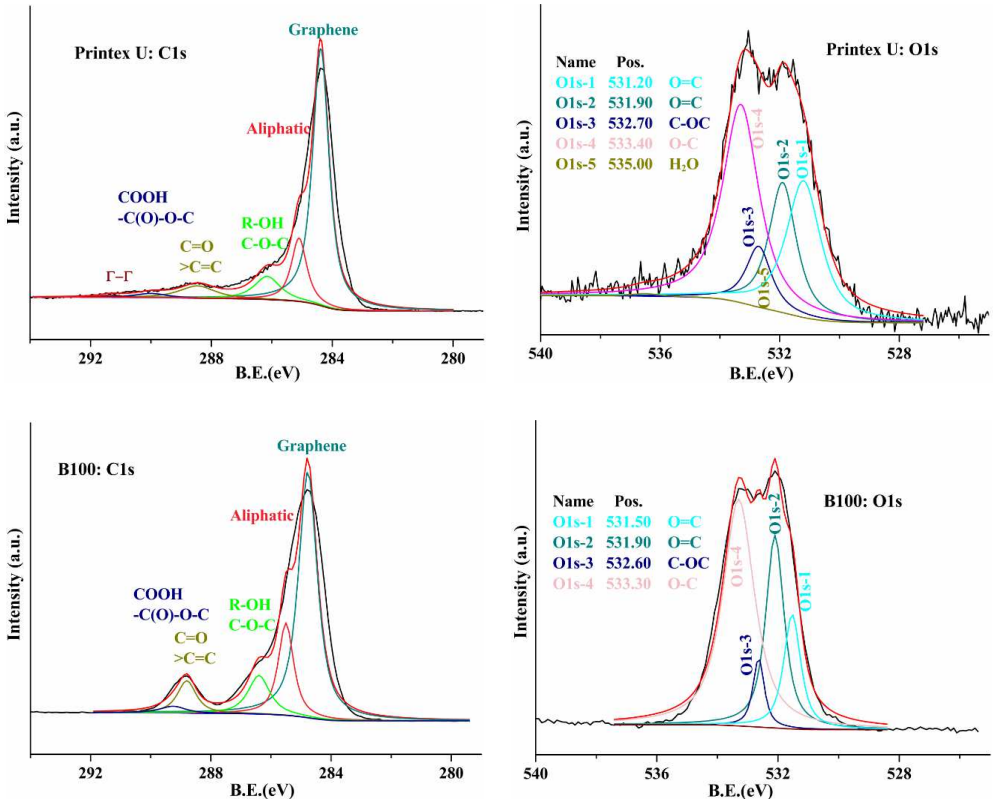

Fig. 12. XP spectra of C1s, O1s of the raw Printex U and B100 samples.

Table 6. XPS results of Printex U and B100 samples.

Samples	Printex U (at.%)			B100 (at.%)		
	C	O	Graphene	C	O	Graphene
Raw soot	90.3	9.7	59.4	80.9	19.1	49.1
Soot-500	90.1	9.9	54.6	80.3	19.7	42.0
Soot-600	89.2	10.8	45.1	78.0	22.0	37.7

Fig. 12 presents the XP spectra of the raw Printex U and B100 samples in the C 1s and O 1s energy regions, and those of the activated soot samples are shown in Fig. S6 and Fig. S7. It can be clearly seen in C 1s XPS that these soot samples mainly consist of graphene, aliphatic carbon and molecular carbon (R-OH, C-O-C, -COOH, -C(O)-O-C, -C=O, etc.) [84,85]. These molecular carbon species are also detected in O 1s spectra. Table 6 lists the relative contents of surface elements of the detected soot samples. It can be observed that the real Biodiesel soot shows higher oxygen content and lower content of graphene component than Printex U soot, this indicates

that Biodiesel soot has a higher disorder, which was also confirmed in the previous work [48]. After the soot was activated at different temperatures, the activated soot samples show different XPS results. For both Printex U and B100, the activated samples all show an increased oxygen content and a decreased graphene content. By comparison, soot-600 has a more apparent increase in oxygen content and a larger decrease in graphene carbon than soot-500. Thus, it shows higher structural disorder, this well agrees with the results of both Raman spectroscopy and HRTEM. The result is well correlated with the reactivity of the activated Printex U soot but not with that of the activated B100 soot (Table 1).

3.2.6. DRIFTS

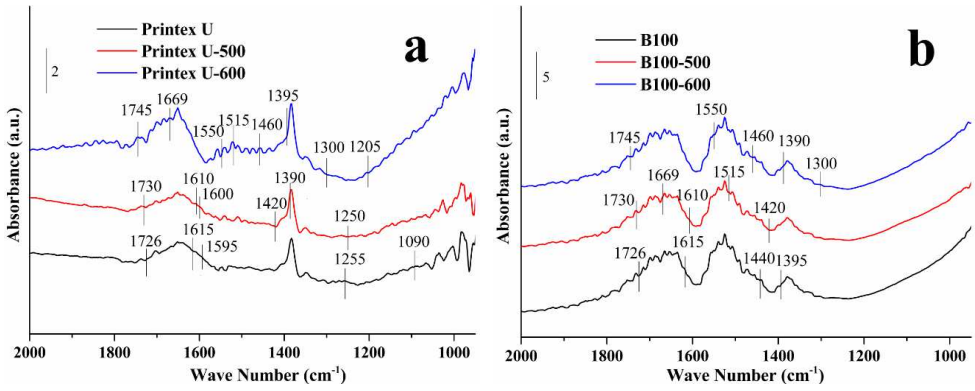

Fig. 13. DRIFTS results of Printex U and B100 samples.

The DRIFT spectra of raw and activated Printex U and B100 soot samples were investigated to obtain more information about oxygen functional groups on the carbon surface. The obtained IR spectra are shown in Fig. 13. According to the DRIFTS results and the previous reports [87-91], the bands at around 1205 and 1090 cm^{-1} are assigned to the stretching of C-OH and the bands at 1550 and 1420 cm^{-1} are ascribed to the symmetric and asymmetric stretching of COO in the aromatic carboxylate species, as well as some aromatic groups are very likely to be found at around 1515 cm^{-1}. The stretching of C=O in lactones and carboxylic anhydrides can be observed at 1669 and 1745 cm^{-1} as well as that in quinone and ceto-enol groups at 1610 cm^{-1}. The weak band at around 1250 cm^{-1} may be associated with C-O stretching. It was reported that the formation of some surface oxygen complexes (SOCs) could be confirmed at 1730-1750 cm^{-1} (carboxylic anhydrides and lactones), 1595 and 1615

583 cm^{-1} (quinone and ceto-enol groups) as well as 1255 cm^{-1} (ethers and phenols) [86].
584 Moreover, in another publication [30], it was reported that the band at 1726 cm^{-1} is
585 ascribed to the vibration of C=O in aromatic ester groups and the band at 1595 cm^{-1}
586 can be attributed to the stretching vibration of conjugated C=C bonds or the bending
587 mode of H_2O. The apparent absorption bands between 1726 and 1615 cm^{-1} are
588 difficult to assign in details. The bending vibration of C-H is also found at about 1460,
589 1395 and 1390 cm^{-1} [30,87]. The band at 1600 cm^{-1} could be attributed to the
590 presence of H_2O and the bands at 1300-1000 cm^{-1} are assigned to C-O vibrations [30].
591 As shown in Fig. 13, the real Biodiesel soot B100 exhibits more surface oxygen
592 functional components than Printex U soot in view of much stronger absorption
593 signals, especially for the surface components (such as aromatic groups) appearing at
594 1600-1400 cm^{-1}. This result would give a better explanation for the XPS result that
595 B100 soot exhibits higher oxygen content and lower carbon content than Printex U. In
596 Fig. 13a, it can be seen that the IR result of Printex U-500 seems to be similar with
597 that of raw Printex U, but an apparent change can be observed for Printex U-600 with
598 an increased absorbance signal. This illustrates that the contents of surface functional
599 groups, for example, aromatic groups (1550, 1515, 1460 and 1420 cm^{-1}), C-H (1460,
600 1395 and 1390 cm^{-1}) and C=O (1750-1726 cm^{-1}), visibly increase on the surface of
601 Printex U-600. It is also noted that the C=C components of Printex U-600 obviously
602 decrease compared to raw and Printex U-500 soot. The previous XPS results reveal
603 that Printex U-600 shows more apparent changes in oxygen and graphene contents
604 than Printex U-500, relative to raw soot. The IR results here would be a reasonable
605 explanation for this point. Besides, in Fig. 13b, Compared with raw B100, B100-600
606 exhibits a similar IR result and B100-500 has a slightly decreased IR signal. This
607 indicates that there is no an obvious change in surface oxygen functional species for
608 the raw and activated Biodiesel soot.
609
610 *3.3. Correlation of structural and surface properties to reactivity*
611 Many authors have analyzed the relationship between soot structure and oxidative
612 reactivity by using XRD, Raman and HRTEM characterizations and found that the
613 reactivity of soot depends on its structural properties, i,e. length scale, amorphous

carbon, the degree of graphitization, nanoparticle size and surface morphology [29,38,40,47,73,90]. Wu et al. [86] studied the surface organic components (such as aromatic carboxylate, carboxylic anhydrides and lactones) of soot during soot combustion in the presence of catalysts through DRIFTS tests and summarized that the catalytic reactivity of soot is related to the concentration of surface organic components. Müller et al. [30] investigated the correlation of the non-catalytic reactivity of different soot samples to surface functional groups characterized by DRIFTS measurements and confirmed an important role of the functionalization on the onset of soot combustion.

Fig. 6 and Fig. 7 reveal that all the activated Printex U and Biodiesel soot samples present an increase in particles aggregates size. The previous study has discussed the relationship between particles aggregates size and soot reactivity, being found that smaller particles aggregates are more reactive than larger ones [48]. The result in the present work cannot illustrate this point. For example, the activated soot Printex U-600 exhibits the best reactivity in both O_2 and NO + O_2, but its mean particles aggregates size is the largest one. This might indicate that smaller soot particles aggregates have been oxidized during the activation. In the case of Biodiesel soot samples, the activated soot shows a decreased low-temperature reactivity (Fig. 3), this may be attributed to the loss of smaller particles aggregates.

It was reported that high surface area of soot could benefit to improve its oxidative reactivity [85]. The previous BET results reveal that the activation of soot samples increases their specific surface area. Thus, the activated Printex U soot samples, especially for Printex U-600, show an apparent enhancement in both non-catalytic and catalytic reactivity. However, this is not evident for Bio soot samples in correlating surface area to their reactivity. On the contrary, in the case of isothermal reactions at 350 °C, the activated Bio soot samples exhibit an increase in their "final oxidation rate" under NO + O_2 (Table 3), which can be well correlated with their increased surface area.

Raman spectroscopy is an important method to study nanostructural features of soot, D1 band FWHM and the relative intensity of D3 band (I_{D3}/I_G) were reported to be the main parameters to evaluate soot structure [28,29]. Thus, Fig. 14 presents the

correlation of the reactivities (T_m) of Printex U and B100 samples with structural features. For Printex U samples, as shown in Fig. 14, the two activated soot samples (Printex U-500 and -600) show similar and higher D1 band FWHM and I_{D3}/I_G ratios, revealing their increased disorder structure. However, the non-catalytic and catalytic reactivities of soot in O_2 follow the order: Printex U-600 > Printex U-500 ≈ Printex U and the catalytic reactivity in NO + O_2 follows the order: Printex U-600 > Printex U-500 > Printex U. This result cannot be well correlated to Raman parameters. Besides, in previous HRTEM results, it can be observed that the degree of graphitization changes with the order: Printex U-600 < Printex U-500 < Printex U. The content of graphene carbon on the surface of Printex U samples also follows this order (Fig. 15). The results can well agree with the catalytic reactivity in NO + O_2. On the other hand, Fig. 15 shows that the order of surface oxygen content of Printex U samples is Printex U-600 (10.8%) > Printex U-500 (9.9%) ≈ Printex U (9.7%). The previous DRIFTS results also reveal that Printex U and Printex U-500 have close quantities of surface functional groups and Printex U-600 has an apparent increase in that compared to them. These conclusions are well correlated to the non-catalytic and catalytic reactivities of soot in O_2.

In the case of B100 soot samples, as shown in Fig. 14 and Fig. 15, it can be known that the non-catalytic reactivity in O_2 follows the order: B100 ≈ B100-500 < B100-600 and the catalytic reactivities in both O_2 and NO + O_2 follow the order: B100-500 < B100 ≈ B100-600. It is also observed in Fig. 14 that B100-500 shows lower D1 FWHM value than B100 and B100-600, indicating an increase in graphitic order, which seems to be correlated to the catalytic reactivity. The I_{D3}/I_G ratio of B100-500 exhibits a slightly increased value than that of B100 and B100-600, this indicates higher content of amorphous carbon in B100-500 soot. However, that cannot agree with the reactivity. In the previous discussion on Raman results, it was mentioned that it might be difficult to analyze the nanostructure of soot by only using Raman. The HRTEM results reveal that the activated soot samples show a higher disorder than the raw B100. In Fig. 15, the XPS results also indicate that the contents of surface graphene carbon and oxygen follow the order: B100 > B100-500 > B100-600. But these results cannot be well correlated to the reactivity of B100

samples. On the other side, it is noted in Fig. 13b that B100 and B100-600 show similar DRIFT spectra and slightly higher concentration of surface functional groups than B100-500, which is well correlated to their reactivities.

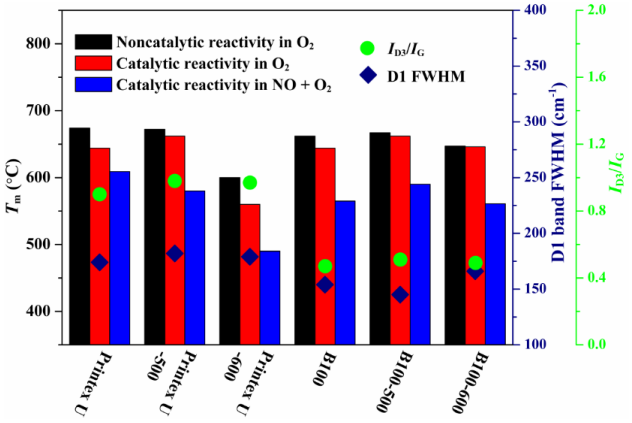

Fig. 14. Correlation of the non-catalytic and catalytic reactivities of Printex U and B100 with Raman parameters including D1 band FWHM and I_{D3}/I_G.

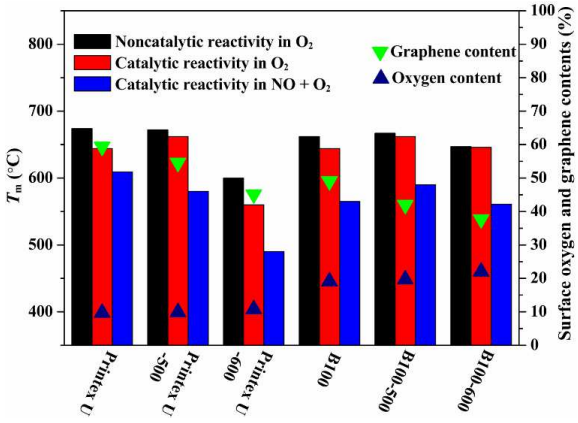

Fig. 15. Correlation of the non-catalytic and catalytic reactivities of Printex U and B100 with surface oxygen and graphene contents obtained by XPS.

In fact, it is difficult to correlate structural and surface properties to the reactivity of soot, because the factors that affect soot oxidative reactivity are complex, not only related to the structure and surface property but also to soot oxidation reaction conditions. For example, in the previous isothermal reactions at 350 °C under O_2, the soot oxidation rates of raw and activated Printex U and B100 follow the order: Printex U (0.0082 $\mu mol_{soot}/s/g_{cat.}$) ≈ Printex U-500 (0.0082 $\mu mol_{soot}/s/g_{cat.}$) < Printex U-600 (0.0538 $\mu mol_{soot}/s/g_{cat.}$) and B100 (0.0814 $\mu mol_{soot}/s/g_{cat.}$) > B100-500 (0.0243 $\mu mol_{soot}/s/g_{cat.}$) ≈ B100-600 (0.0243 $\mu mol_{soot}/s/g_{cat.}$), respectively. However, under NO

695 + O_2, their oxidation reaction rates all follow the order: raw soot < soot-500 <
696 soot-600. It is also noticed that the isothermal reaction rates under NO + O_2 can be
697 well correlated to HRTEM and XPS results. Moreover, some authors tried to link the
698 nanostructure characterized by Raman to soot oxidative reactivity and found there
699 was no an apparent relationship between the reactivity and Raman results [48,92]. In
700 this work, similarly, the Raman results cannot be also well correlated to the reactivity
701 of soot. But some researchers also confirmed that the nanostructure analyzed by
702 Raman is one of the factors that determine the oxidation reactivity of soot [28,29,90].
703 It was also reported that the reactivity of soot is not only related to the nanostructure
704 but to soot composition [80,84,93], oxygen content [49] and surface functional groups
705 [30,91]. Thus, a co-influence of various factors should be considered in analyzing
706 soot oxidative reactivity.
707 Besides, in real applications of aftertreatment technology, the activation of Diesel
708 soot by partial oxidation with O_2 will take place during soot accumulation and DPF
709 regeneration. The activating process influencing physicochemical properties and the
710 reactivity of soot should be studied, because this is very useful for understanding DPF
711 regeneration and optimizing aftertreatment technology. This study gives valuable
712 findings on the changes in the structure, surface and non-catalytic/catalytic reactivity
713 of Printex U model and real Bio soot before and after the activation. In comparison,
714 the two types of soot show different changing trends. Many researchers often use
715 Printex U model to investigate the oxidative reactivity of Diesel soot, this might not
716 confirm the real case of the combustion of Diesel soot produced from vehicles'
717 engines. This would require to select more suitable model soot in experimental studies.
718 Furthermore, this work also reveals that the activation of soot is an important factor
719 that affects DPF regeneration. Thus, the changes in soot structure and surface during
720 soot combustion should be also concerned in future study.
721
722 **4. Conclusions**
723 The present work studied and compared the structure, surface and reactivity of the
724 activated Printex U model and real Bio soot samples through a series of
725 characterizations and TPO measurements. In the case of model soot Printex U, it was

confirmed that the activated samples exhibited an apparently increased reactivity especially under NO + O_2. The result should be related to their higher surface area, higher disorder structure, increased surface oxygen content and surface functional groups, determined by BET, Raman, HRTEM, XPS and DRIFTS. On the other hand, after the activation of real Bio soot, TPO results revealed that there was no an obvious enhancement in the reactivity and even the ignition (T_i) occurred at higher temperature. This could not well correlated with the structure and surface evolving towards higher disorder and oxygen content. However, the isothermal reactions under NO + O_2 had a good correlation with the structure and surface. Besides, HRTEM indicated different oxidation routes of Printex U and Biodiesel soot. An important finding in this work is to reveal the impact of the activation during soot accumulation and DPF regeneration on the structure, surface and reactivity of Diesel soot, and present the different trends of model and real Bio soot. It will provide some important information in understanding and optimizing DPF regeneration.

References

[1] Reşitoğlu IA, Altinişik K, Keskin A. The pollutant emissions from diesel-engine vehicles and exhaust aftertreatment systems, Clean Technol Environ Policy 2015;17:15-27.

[2] Twigg MV. Progress and future challenges in controlling automotive exhaust gas emissions. Appl Catal B 2007;70:2-15.

[3] Giechaskiel B, Alföldy B, Drossinos Y. A metric for health effects studies of diesel exhaust particles. Aerosol Sci 2009;40:639-51.

[4] Zhou HQ, Li XR, Zhao WH, Liu FS. Effects of separated swirl combustion chamber geometries on the combustion and emission characteristics of DI diesel engines. Fuel 2019;253:488-500.

[5] Carslaw KS, Boucher O, Spracklen DV, Mann GW, Rae JG, Woodward S, et al. A review of natural aerosol interactions and feedbacks within the earth system. Atmos Chem Phys 2010;10:1701-37.

[6] Mahowald N, ward DS, Kloster S, Flanner MG, Heald CL, Heavens NG, et al. Aerosol impacts on climate and biogeochemistry. Annu Rev Environ Resour 2011;36: 45-74.

[7] Niessner R. The many faces of soot: characterization of soot nanoparticles produced by

757 engines. Angew Chem Int Ed 2014;53:12366-79.
758 [8] Geng P, Yao C, Wang Q, Wei L, Liu J, Pan W, Han G. Effect of DMDF on the PM emission
759 from a turbo-charged diesel engine with DDOC and DPOC. Appl Energy 2015;148:449-55.
760 [9] Liu ZG, Ottinger NA, Cremeens CM. Vanadium and tungsten release from V-based selective
761 catalytic reduction diesel aftertreatment. Atmos Environ 2015;104:154-61.
762 [10] Mei DQ, Zhu ZN, Mei CW, Chen Z, Yuan YN. Fractal morphology features and carbon
763 component analysis of diesel particulates. Environ Sci Pollut Res 2019;26:14014-23.
764 [11] Roy R, Jan R, Gunjal G, Bhor R, Pai K, Satsangi PG. Particulate matter bound polycyclic
765 aromatic hydrocarbons: Toxicity and health risk assessment of exposed inhabitants. Atmos
766 Environ 2019;210:47-57.
767 [12] Kumar SN, Verma P, Bastia B, Jain S. AK health risk assessment of polycyclic aromatic
768 hydrocarbons: a review. J Pathol Toxicol 2014;1:16-30.
769 [13] Lin YC, Li YC, Shangdiar S, Chou FC, Sheu YT, Cheng PC. Assessment of $PM_{2.5}$ and PAH
770 content in $PM_{2.5}$ emitted from mobile source gasoline-fueled vehicles in concomitant with the
771 vehicle model and mileages. Chemosphere 2019;226:502-8.
772 [14] European Parliament. Regulation (EC) No 715/2007 of the European Parliament and the
773 Council of 20 June 2007 on type approval of motor vehicles with respect to emissions from light
774 passenger and commercial vehicles (Euro 5 and Euro 6) and on access to vehicle repair and
775 maintenance information, O.J. L171/1 (2007).
776 [15] European Commission. Commission Regulation No 582/2011 of 25 May 2011 implementing
777 and amending Regulation (EC) No 595/2009 of the European Parliament and of the Council with
778 respect to emissions from heavy duty vehicles (Euro VI) and amending Annexes I and III to
779 Directive 2007/46/EC of the European Parliament and of the Council, O.J. L167/1 (2011).
780 [16] European Commission. Commission Regulation (EU) No 459/2012 of 29 May 2012
781 amending Regulation (EC) No 715/2007 of the European Parliament and of the Council and
782 Commission Regulation (EC) No 692/2008 as regards emissions from light passenger and
783 commercial vehicles (Euro 6), O.J. L142/16 (2012).
784 [17] Zhong H, Tan J, Wang YL, Tian JL, Hu NT, Cheng J, Zhang XM. Effects of a Diesel
785 particulate filter on emission characteristics of a China II non-road Diesel engine. Energy Fuels
786 2017;31:9833-39.
787 [18] Bensaid S, Marchisio DL, Fino D. Numerical simulation of soot filtration and combustion

788 within diesel particulate filters. Chem Eng Sci 2010;65:357-63.
789 [19] Mokhri MA, Abdullah NR, Abdullah SA, Kasalong S, Mamat R. Soot filtration recent
790 simulation analysis in diesel particulate filter (DPF). Procedia Eng 2012;41:1750-5.
791 [20] Caliskan H, Mori K. Environmental, enviroeconomic and enhanced thermodynamic analyses
792 of a diesel engine with diesel oxidation catalyst (DOC) and diesel particulate filter (DPF) after
793 treatment systems. Energy 2017;128:128-44.
794 [21] Lee J, Theis JR, Kyriakidou EA. Vehicle emissions trapping materials: Successes, challenges,
795 and the path forward. Appl Catal B 2019;243:397-414.
796 [22] Shao SS, Cheng JN, Zhang B, Ma NJ, Zhang DX, Wang YL, et al. Effects of a DOC plus
797 DPF system on emission characteristics of China Pi engineering vehicle diesel engine and
798 influence factors of trapping efficiency of PM for DOC plus DPF system. Energy Source Part A
799 2019;41:527-41.
800 [23] Liu S, Wu XD, Weng D, Li M, Fan J. Sulfation of Pt/Al_2O_3 catalyst for soot oxidation: High
801 utilization of NO_2 and oxidation of surface oxygenated complexes. Appl Catal B
802 2013;138-139:199-211.
803 [24] Jeguirim M, Tschamber V, Ehrburger P. Catalytic effect of platinum on the kinetics of carbon
804 oxidation by NO_2 and O_2. Appl Catal B 2007;76:235-40.
805 [25] Leistner K, Nicolle A, Costa PD. Impact of the catalyst/soot ratio on diesel soot oxidation
806 pathways. Energy Fuels 2012;26:6091-7.
807 [26] Zhang HL, Hu W, Zhou CX, Liu HR, Yao P, Wang JL, et al. A new understanding of
808 CeO_2-ZrO_2 catalysts calcinated at different temperatures: Reduction property and soot-O_2 reaction.
809 Appl Catal A 2018;563:204-15.
810 [27] Zhang HL, Hou ZY, Zhu Y, Wang JL, Chen YQ. Sulfur deactivation mechanism of
811 Pt/MnO_x-CeO_2 for soot oxidation: Surface property study. Appl Surf Sci 2017;396:560-5.
812 [28] Knauer M, Schuster ME, Su DS, Schlögl R, Niessner R, Ivleva NP. Soot structure and
813 reactivity analysis by Raman microspectroscopy, Temperature-Programmed Oxidation and
814 High-resolution transmission electron microscopy. J Phys Chem A 2009;113:13871-80.
815 [29] Lapuerta M, Oliva F, Agudelo JR, Boehman AL. Effect of fuel on the soot nanostructure and
816 consequences on loading and regeneration of diesel particulate filters. Combust Flame
817 2012;159:844-53.
818 [30] Müller JO, Su DS, Jentoft RE, Kröhnert J, Jentoft FC, Schlögl R. Morphology-controlled

819 reactivity of carbonaceous materials towards oxidation. Catal Today 2005;102-103:259-65.
820 [31] Abboud J, Schobing J, Legros G, Matynia A, Bonnety J, Tschamber V, et al. Impacts of
821 ester's carbon chain length and concentration on sooting propensities and soot oxidative reactivity:
822 Application to Diesel and Biodiesel surrogates. Fuel 2018;222:588-98.
823 [32] Lamharess N, Starck L, Millet CN, Costa PD. Effect of biofuels on catalyzed diesel
824 particulate filter regeneration. Top Catal 2013;56:462-6.
825 [33] Hansen BB, Jensen AD, Jensen PA. Performance of diesel particulate filter catalysts in the
826 presence of biodiesel ash species. Fuel 2013;106:234-40.
827 [34] Al-Qurashi K, Boehman AL. Impact of exhaust gas recirculation (EGR) on the oxidative
828 reactivity of diesel engine soot. Combust Flame 2008;155:675-95.
829 [35] Yehliu K, Armas O, Vander Wal RL, Boehman AL. Impact of engine operating modes and
830 combustion phasing on the reactivity of diesel soot. Combust Flame 2013;160:682-91.
831 [36] Hori S, Sato T, Narusawa K. Effects of diesel fuel composition on SOF and PAH exhaust
832 emissions. JSAE Review 1997;18:255-61.
833 [37] Kain J. Connecticut diesel emissions control technologies forum, Retrofit Overview. August
834 17, 2005.
835 [38] Sadezky A, Muckenhuber H, Grothe H, Niessner R, Pöschl U. Raman microspectroscopy of
836 soot and related carbonaceous materials: spectral analysis and structural information. Carbon
837 2005;43:1731-42.
838 [39] Setten B, Makkee M, Moulijn JA. Science and technology of catalytic diesel particulate
839 filters. Catal. Rev. 2001;43:489-564.
840 [40] Vander Wal RL, Tomasek AJ. Soot oxidation: dependence upon initial nanostructure.
841 Combust Flame 2003;134:1-9.
842 [41] Alfe M, Apicella B, Barbella R, Rouzaud JN, Tregrossi A, Ciajolo A. Structure-property
843 relationship in nanostructures of young and mature soot in premixed flames. P Combust Inst
844 2009;32:697-704.
845 [42] Ishiguro T, Suzuki N, Fujitani Y, Morimoto H. Microstructural changes of Diesel soot during
846 oxidation. Combust Flame 1991;85:1-6.
847 [43] Wang XC, Wang Y, Bai YQ, Wang P, Wang DX, Guo FN. Effects of 2,5-dimethylfuran
848 addition on morphology, nanostructure and oxidation reactivity of diesel exhaust particles. Fuel
849 2019;253:731-40.

850 [44] Schobing J, Tschamber V, Brillard A, Leyssens G, Iojoiu E, Lauga V. Impact of engine
851 operating cycle, biodiesel blends and fuel impurities on soot production and soot characteristics.
852 Combust Flame 2018;198:1-13.
853 [45] Yehliu K, Vander Wal RL, Armas O, Boehman AL. Impact of fuel formulation on the
854 nanostructure and reactivity of diesel soot. Combust Flame 2012;159:3597-606.
855 [46] Barrientos EJ, Maricq MM, Boehman AL, Andersson JE. Impact of ester structures on the
856 soot characteristics and soot oxidative reactivity of biodiesel. SAE Technical Paper 2015-01-1080
857 (2015).
858 [47] Boehman AL, Song J, Alam M. Impact of biodiesel blending on diesel soot and the
859 regeneration of particulate filters. Energy Fuels 2005;19:1857-64.
860 [48] Zhang HL, Pereira O, Legros G, Iojoiu EE, Galvez ME, Chen YQ, et al. Structure-reactivity
861 study of model and Biodiesel soot in model DPF regeneration conditions. Fuel 2019;239:373-86.
862 [49] Seong HJ, Boehman AL. Studies of soot oxidative reactivity using a diffusion flame burner.
863 Combust Flame 2012;159:1864-75.
864 [50] Song J, Alam M, Boehman AL. Impact of alternative fuels on soot properties and DPF
865 regeneration. Combust Sci Technol 2007;179:1991-2037.
866 [51] Verma P, Pickering E, Jafari M, Guo Y, Stevanovic S, Fernando JFS, et al. Influence of
867 fuel-oxygen content on morphology and nanostructure of soot particles. Combust Flame
868 2019;205:206-19.
869 [52] Corro G, Flores A, Pacheco-Aguirre F, Pal U, Banuelos F, Ramirez A, et al.. Biodiesel and
870 fossil-fuel diesel soot oxidation activities of Ag/CeO_2 catalyst. Fuel 2019;250:17-26.
871 [53] Wei Y, Zhao Z, Jin B, Yu X, Jiao J, Li K, et al.. Synthesis of AuPt alloy nanoparticles
872 supported on 3D ordered macroporous oxide with enhanced catalytic performance for soot
873 combustion. Catal Today 2015;251:103-13.
874 [54] Dhal GC, Dey S, Mohan D, Prasad R. Study of Fe, Co, and Mn-based perovskite-type
875 catalysts for the simultaneous control of soot and NO_x from diesel engine exhaust. Mater
876 Discovery 2017;10:37-42.
877 [55] Mishra A, Prasad R. Preparation and application of perovskite catalysts for diesel soot
878 emissions control: an overview. Catal Rev 2014;56:57-81.
879 [56] Bueno-López A, Krishna K, Makkee M, Moulijn JA. Enhanced soot oxidation by lattice
880 oxygen via La^{3+}-doped CeO_2. J Catal 2005;230:237-48.

881 [57] Tikhomirov K, Kröcher O, Elsener M, Wokaun A. MnO_x-CeO_2 mixed oxides for the
882 low-temperature oxidation of diesel soot. Appl Catal B 2006;64:72-78.
883 [58] Zhang HL, Yuan SD, Wang JL, Gong MC, Chen YQ. Effects of contact model and NO_x on
884 soot oxidation activity over Pt/MnO_x-CeO_2 and the reaction mechanisms. Chem Eng J
885 2017;327:1066-76.
886 [59] Bassou B, Guilhaume N, Iojoiu EE, Farrusseng D, Lombaert K, Bianchi D, Mirodatos C.
887 High-throughput approach to the catalytic combustion of diesel soot II: Screening of oxide-based
888 catalysts. Catal Today 2011; 159: 138-143.
889 [60] Zhu L, Yu J, Wang X. Oxidation treatment of diesel soot particulate on $Ce_xZr_{1-x}O_2$. J Hazard
890 Mater 2007;140:205-10.
891 [61] Yang ZZ, Hu W, Zhang N, Li Y, Liao YW. Facile synthesis of ceria-zirconia solid solutions
892 with cubic-tetragonal interfaces and their enhanced catalytic performance in diesel soot oxidation.
893 J Catal 2019; in press, DOI: 10.1016/j.jcat.2019.06.029.
894 [62] Aneggi E, Leitenburg C, Trovarelli A. On the role of lattice/surface oxygen in ceria-zirconia
895 catalysts for diesel soot combustion. Catal Today 2012;181:108-15.
896 [63] Atribak I, Bueno-López A, García-García A. Role of yttrium loading in the physico-chemical
897 properties and soot combustion activity of ceria and ceria-zirconia catalysts. J Mol Catal A: Chem
898 2009;300:103-10.
899 [64] Zhang HL, Wang JL, Zhang YH, Jiao Y, Ren CJ, Gong MC, et al. A study on H_2-TPR of
900 Pt/$Ce_{0.27}Zr_{0.73}O_2$ and Pt/$Ce_{0.27}Zr_{0.70}La_{0.03}O_x$ for soot oxidation. Appl Surf Sci 2016;377:48-55.
901 [65] Oi-Uchisawa J, Obuchi A, Ogata A, Enomoto R, Kushiyama S. Effect of feed gas
902 composition on the rate of carbon oxidation with Pt/SiO_2 and the oxidation mechanism. Appl
903 Catal B 1999;21:9-17.
904 [66] Yamazaki K, Kayama T, Dong F, Shinjoh H. A mechanism study on soot oxidation over
905 CeO_2-Ag catalyst with 'rice-ball' morphology. J Catal 2011;282:289-98.
906 [67] Liu S, Wu XD, Liu W, Chen WM, Ran R, Li M, et al. Soot oxidation over CeO_2 and Ag/CeO_2:
907 Factors determining the catalyst activity and stability during reaction. J Catal 2016;337:188-98.
908 [68] Lin F, Wu XD, Liu S, Weng D, Huang YY. Preparation of MnO_x-CeO_x-Al_2O_3 mixed oxides
909 for NO_x-assisted soot oxidation: Activity, structure and thermal stability, Chem Eng J
910 2013;226:105-12.
911 [69] Zhang HL, Zhou CX, Galvez ME, Costa PD, Chen YQ. MnO_x-CeO_2 mixed oxides as the

912 catalyst for NO-assisted soot oxidation: The key role of NO adsorption/desorption on catalytic
913 activity, Appl Surf Sci 2018;462:678-84.
914 [70] Zhang HL, Li SS, Lin QJ, Feng X, Chen YQ, Wang JL. Study on hydrothermal deactivation
915 of Pt/MnO_x-CeO_2 for NO_x-assisted soot oxidation: redox property, surface nitrates, and oxygen
916 vacancies, Environ Sci Pollut Res 2018;25:16061-70.
917 [71] Pajdowski P, Puchalka B. The process of diesel particulate filter regeneration under real
918 driving conditions. IOP Conf Ser: Earth Environ Sci 2019;214:012114.
919 [72] Seong H, Choi S. Oxidation-derived maturing process of soot, dependent on O_2-NO_2
920 mixtures and temperatures. Carbon 2015;93:1068-76.
921 [73] Abboud J, Schobing J, Legros G, Bonnety J, Tschamber V, Brillard A, et al. Impacts of
922 oxygenated compounds concentration on sooting propensities and soot oxidative reactivity:
923 Application to Diesel and Biodiesel surrogates. Fuel 2017;193:241-53.
924 [74] Wang Y, Alsmeyer DC, McCreery RL. Raman spectroscopy of carbon materials: structural
925 basis of observed spectra. Chem Mater 1990;2:557-63.
926 [75] Cuesta A, Dhamelincourt P, Laureyns J, Martinez-Alonso A, Tascon JMD. Raman
927 microprobe studies on carbon materials. Carbon 1994;32:1523-32.
928 [76] Sze SK, Siddique N, Sloan JJ, Escribano R. Raman spectroscopic characterisation of
929 carbonaceous aerosol. Atmos Environ 2001;35;561-8.
930 [77] Jawhari T, Roid A, Casado J. Raman spectroscopic characterisation of some commercially
931 available carbon black materials. Carbon 1995;33:1561-5.
932 [78] Dippel B, Jander H, Heintzenberg J. NIR FT Raman spectroscopic study of flame soot. Phys
933 Chem Phys 1999;1:4707-12.
934 [79] Nakamura K, Fujitsuka M, Kitajima M. Disorder-induced line broadening in first-order
935 Raman scattering from graphite. Phys Rev B 1990;41:12260-3.
936 [80] Lu T, Cheung CS, Huang Z. Size-resolved volatility, morphology, nanostructure, and
937 oxidation characteristics of diesel particulate. Energy Fuels 2012;26:6168-76.
938 [81] Bladt H, Ivleva NP, Niessner R. Internally mixed multicomponent soot: impact of different
939 salts on soot structure and thermo-chemical properties. J Aerosol Sci 2014;70:26-35.
940 [82] Schmid J, Grob B, Niessner R, Ivleva NP. Multiwavelength Raman microspectroscopy for
941 rapid prediction of soot oxidation reactivity. Anal Chem 2011;83:1173-9.
942 [83] Ishiguro T, Takatori Y, Akihama K. Microstructure of diesel soot particles probed by electron

943 microscopy: first observation of inner core and outer shell. Combust Flame 1997;108:231-4.
944 [84] Valero-Romero MJ, García-Mateos FJ, Rodríguez-Mirasol J, Cordero T. Role of surface
945 phosphorus complexes on the oxidation of porous carbons. Fuel Process Technol
946 2017;157:116-26.
947 [85] Schobing J, Tschamber V, Brillard A, Leyssens G. Impact of biodiesel impurities on carbon
948 oxidation in passive regeneration conditions: Influence of the alkali metals. Appl Catal B
949 2018;226:596-607.
950 [86] Wu XD, Lin F, Xu HB, Weng D. Effects of adsorbed and gaseous NO_x species on catalytic
951 oxidation of diesel soot with MnO_x-CeO_2 mixed oxides. Appl Catal B 2010;96:101-9.
952 [87] Escribano VS, López EF, Gallardo-Amores JM, Del C, Martínez H, Pistarino C, et al. A study
953 of a ceria-zirconia-supported manganese oxide catalyst for combustion of Diesel soot particles.
954 Combust Flame 2008;153:97-104.
955 [88] Figueiredo JL, Pereira MFR, Freitas MMA, Órfão JJM. Modification of the surface chemistry
956 of activated carbons. Carbon 1999;37:1379-89.
957 [89] Setiabudi A, Makkee M, Moulijn JA. The role of NO_2 and O_2 in the accelerated combustion
958 of soot in diesel exhaust gases. Appl Catal B 2004;50:185-94.
959 [90] Knauer M, Carrara M, Rothe D, Niessner R, Ivleva NP. Changes in structure and reactivity of
960 soot during oxidation and gasification by oxygen, studied by microRaman spectroscopy and
961 temperature programmed oxidation. Aerosol Sci Technol 2009;43:1-8.
962 [91] Tapia A, Salgado S, Martin P, Villanueva F, García-Contreras R, Cabanas B. Chemical
963 composition and heterogeneous reactivity of soot generated in the combustion of diesel and GTL
964 (Gas-to-Liquid) fuels and amorphous carbon Printex U with NO_2 and CF_3COOH gases. Atmos
965 Environ 2018;177:214-21.
966 [92] Ye P, Sun CX, Lapuerta M, Agudelo J, Vander Wal R, Boehman AL, Toops TJ, Daw S.
967 Impact of rail pressure and biodiesel fueling on the particulate morphology and soot
968 nanostructures from a common-rail turbocharged direct injection diesel engine. Int J Engine Res
969 2016;17:193–208.
970 [93] Bladt H, Schmid J, Kireeva ED, Popovicheva OB, Perseantseva NM, Timofeev MA, et al.
971 Impact of Fe content in laboratory-produced soot aerosol on its composition, structure, and
972 thermo-chemical properties. Aerosol Sci Technol 2012;46:1337-48.

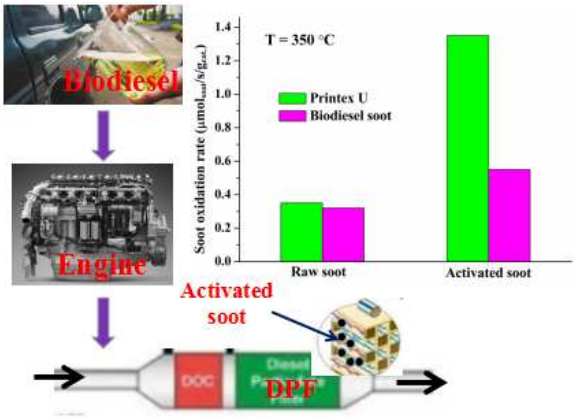
Biodiesel
Engine
T = 350 °C
Printex U
Biodiesel soot
Soot oxidation rate (μmol$_{mol\ s}$/g$_{soot}$)
1.4
1.2
1.0
0.8
0.6
0.4
0.2
0.0
Raw soot
Activated soot
Activated soot
DOC
DPF